Supplementary Information for

In situ ammonium formation mediates efficient hydrogen production from natural seawater splitting

Xiao-Long Zhang[1†], Peng-Cheng Yu [1†], Shu-Ping Sun[1†], Lei Shi[1], Peng-Peng Yang[1], Zhi-Zheng Wu[1], Li-Ping Chi[1], Ya-Rong Zheng[2*], Min-Rui Gao[1*]

[1] Division of Nanomaterials & Chemistry, Hefei National Laboratory for Physical Sciences at the Microscale, University of Science and Technology of China, Hefei 230026, China.

[2] School of Chemistry and Chemical Engineering, Anhui Province Key Laboratory of Value-Added Catalytic Conversion and Reaction Engineering, Anhui Province Engineering Research Center of Flexible and Intelligent Materials, Hefei University of Technology, Hefei, Anhui 230009, China.

Supplementary Figures

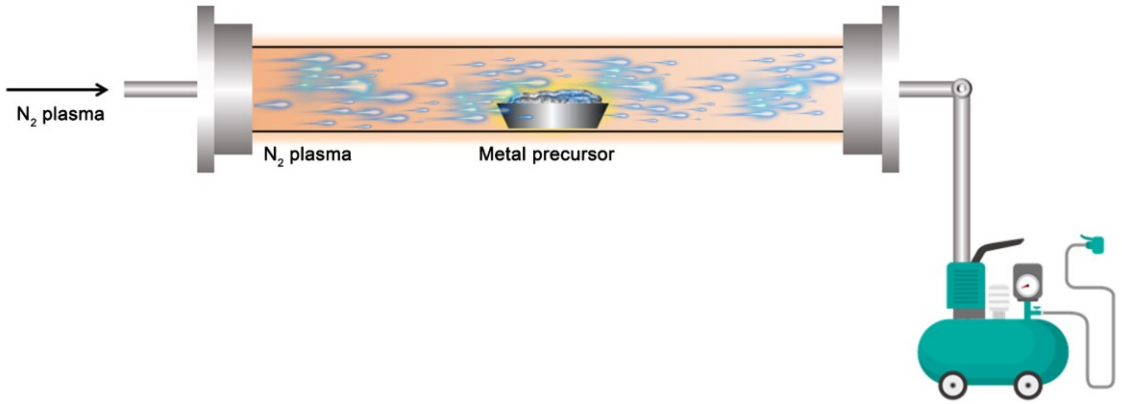

Supplementary Figure 1. Schematic of the RF-PECVD system for the synthesis of metal nitrides. Briefly, the metal powder was subjected to the N_2 plasma treatment in the chamber of the radio frequency-plasma enhanced chemical vapour deposition systems under a pressure of 0.02 Torr. After the temperature of the chamber reached the synthetic temperature, the radio frequency-plasma discharge was conducted at 300 W and 13.56 MHz for 30 min.

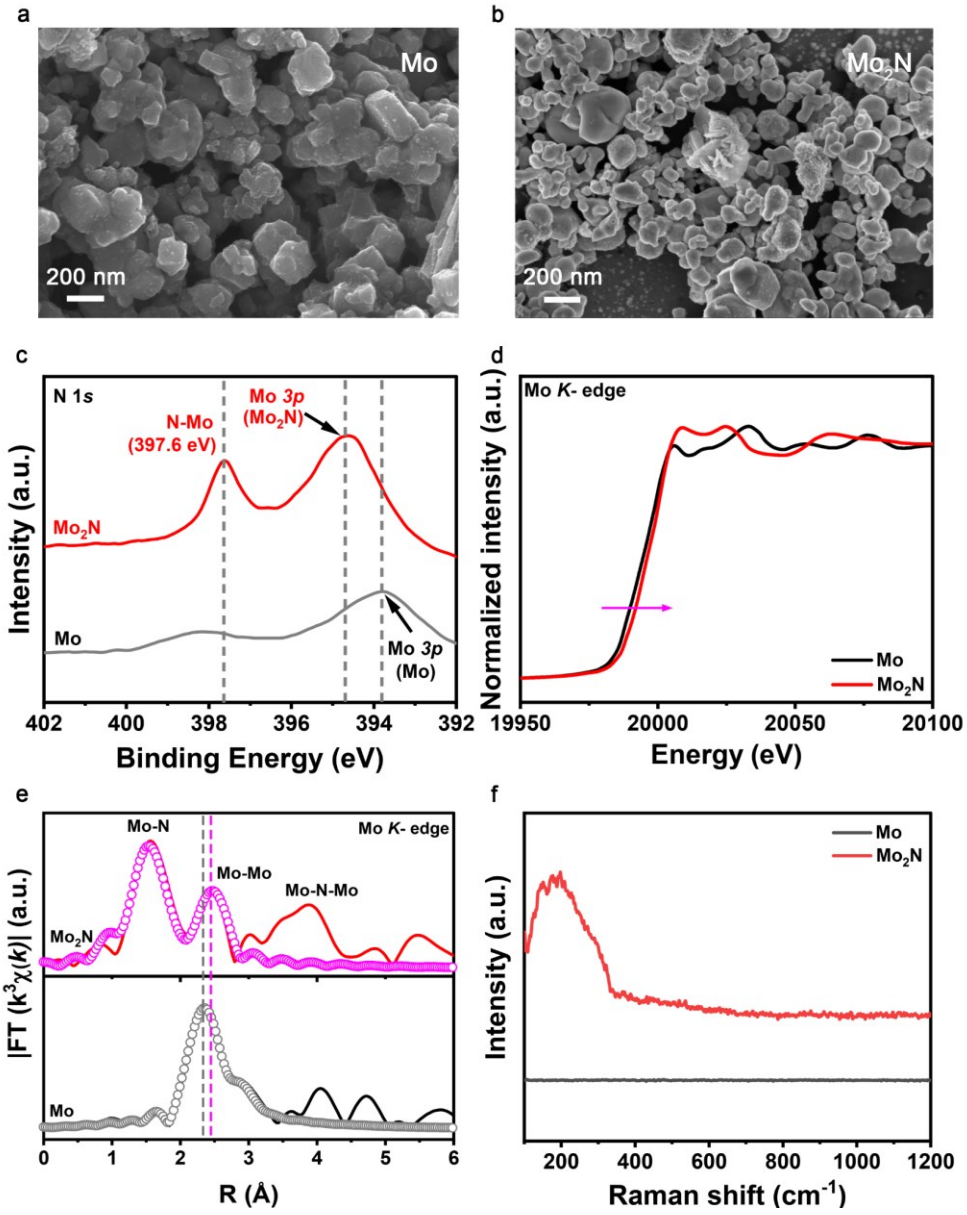

Supplementary Figure 2. Structural characterization of Mo_2N. a, b, SEM images of Mo_2N (**a**) and Mo (**b**). **c,** N 1*s* XPS spectra of Mo_2N and Mo. The N 1*s* peak at 397.6 eV is associated to the typical N-Mo binding energy in the Mo_2N_3 phase, and a peak at 394.7 eV is also detected, corresponding to the Mo 3*p* in the Mo_2N[1]. In addition, the Mo metal show a signal at 393.8 eV, which is ascribed to the Mo $3p$[2]. **d, e,** Mo K-edge XANES (**d**) and corresponding k^3-weighted Fourier transforms spectra (**e**) for Mo and Mo_2N. The adsorption edges of Mo K-edge (**d**) XANES spectra showed that Mo in Mo_2N shifted to higher energy due to the charge transfer from the Mo to N. The EXAFS revealed clear Mo−N bonds for Mo_2N (**e**). The EXAFS analysis also displayed a slight increase in Mo-Mo bond distances after Mo_2N were formed, which was caused by the incorporation of N atoms into the interstitial sites of metals. **f,** The Raman spectrum of Mo_2N and Mo at the Raman laser energy of 4 mW. The Raman spectra of Mo_2N showed a broad band <350 cm^{-1}, which corresponds to the transverse acoustic (TA) and longitudinal acoustic (LA) phonon modes of Mo_2N[3, 4].

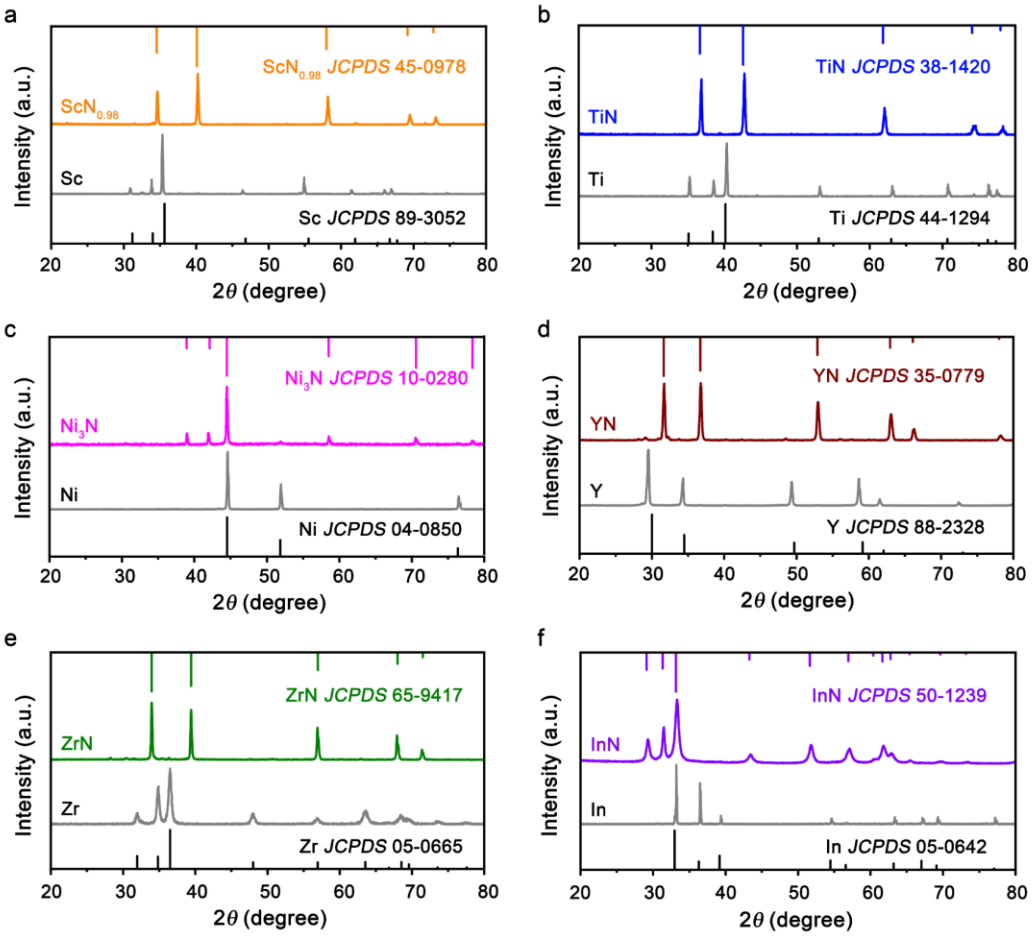

Supplementary Figure 3. X-ray powder diffraction (XRD) patterns. a-f, XRD patterns of different metal nitrides synthesized from respective metal precursors, including $ScN_{0.98}$ (**a**), TiN (**b**), Ni_3N (**c**), YN (**d**), ZrN (**e**), and InN (**f**). The results revealed that the as-synthesized samples were highly crystalline and matched well with the Joint Committee on Powder Diffraction Standards (JCPDS) of corresponding single-phase metal nitrides.

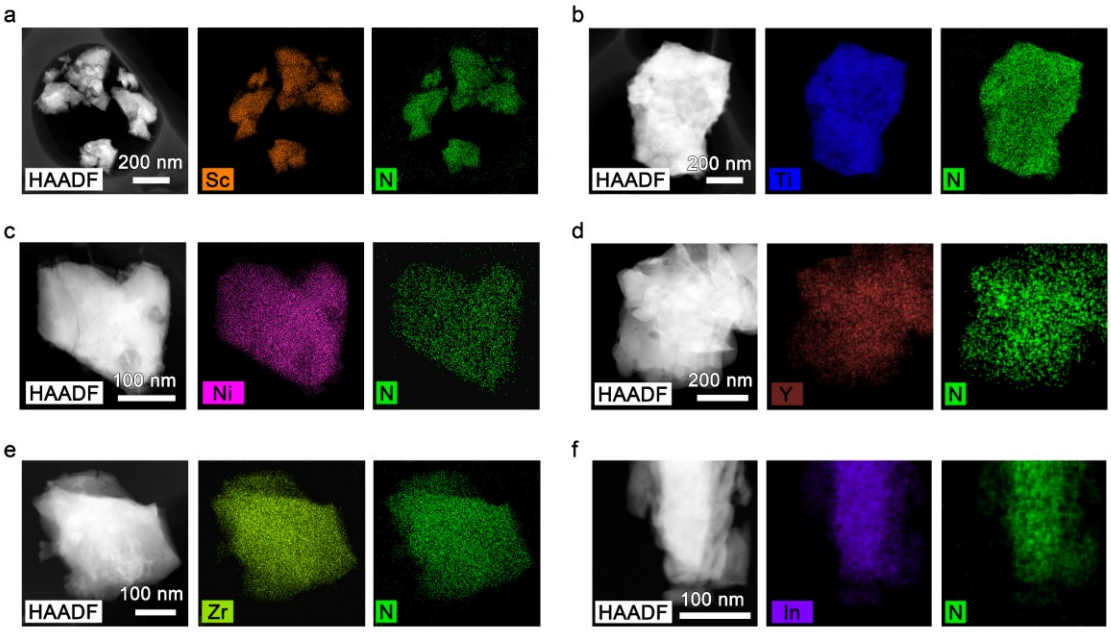

Supplementary Figure 4. STEM-EDX elemental mapping. a-f, The EDX elemental mappings of different metal nitrides synthesized from respective metal precursors, including $ScN_{0.98}$ (**a**), TiN (**b**), Ni_3N (**c**), YN (**d**), ZrN (**e**), and InN (**f**). The EDX elemental mappings exhibited the homogeneous distribution of metal and N element in each metal nitride, respectively.

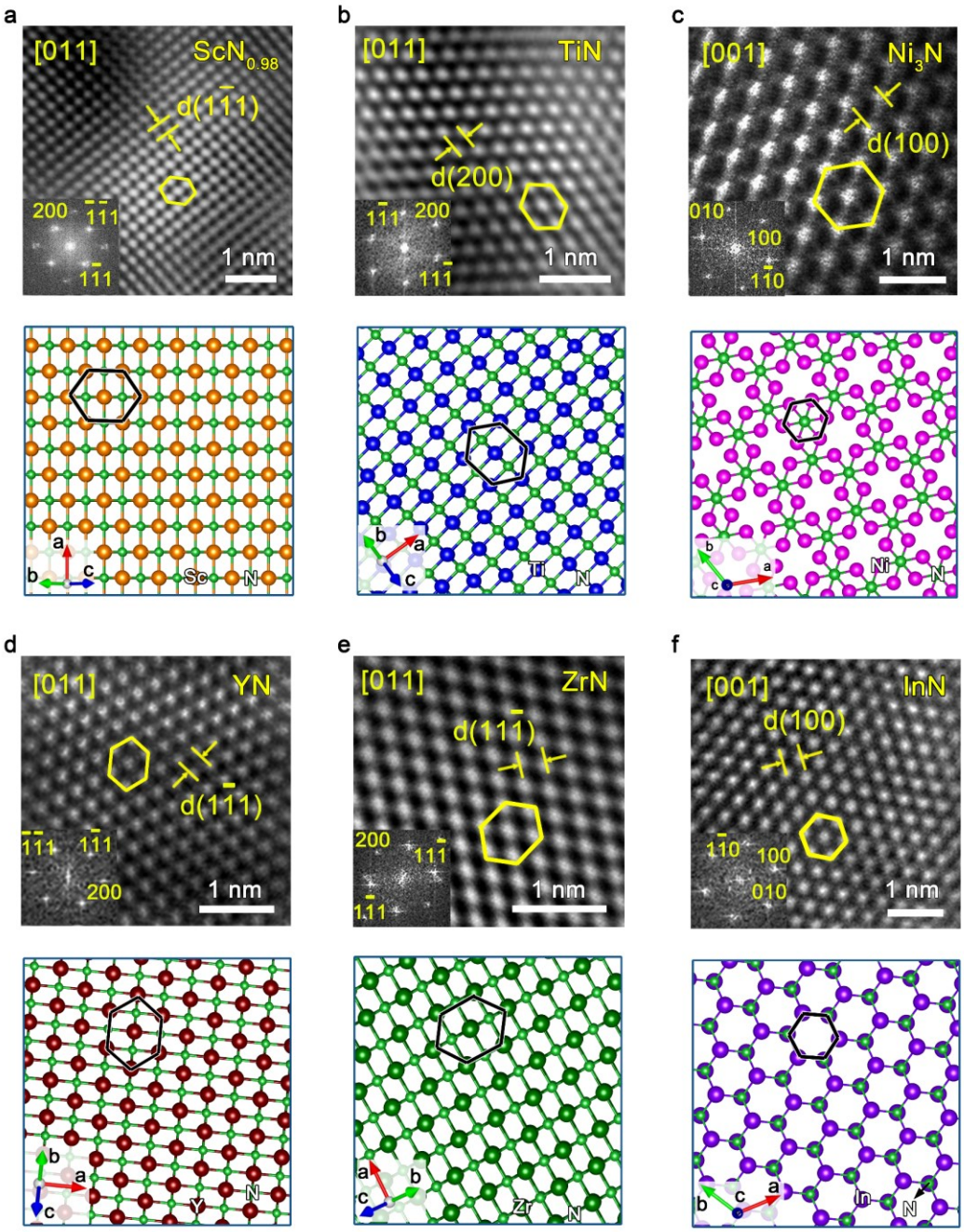

Supplementary Figure 5. HRTEM images. a-f, (**top**) HRTEM images of different metal nitrides synthesized from respective metal precursors, including $ScN_{0.98}$ (**a**), TiN (**b**), Ni_3N (**c**), YN (**d**), ZrN (**e**) and InN (**f**). Inset in each HRTEM image shows corresponding FFT pattern. **a-f,** (**bottom**) Atomic models viewed along the same direction for taking respective HRTEM image. The results show that the well-resolved and continuous lattice fringes were clearly visible, indicative of the high crystallinity of these metal nitride samples.

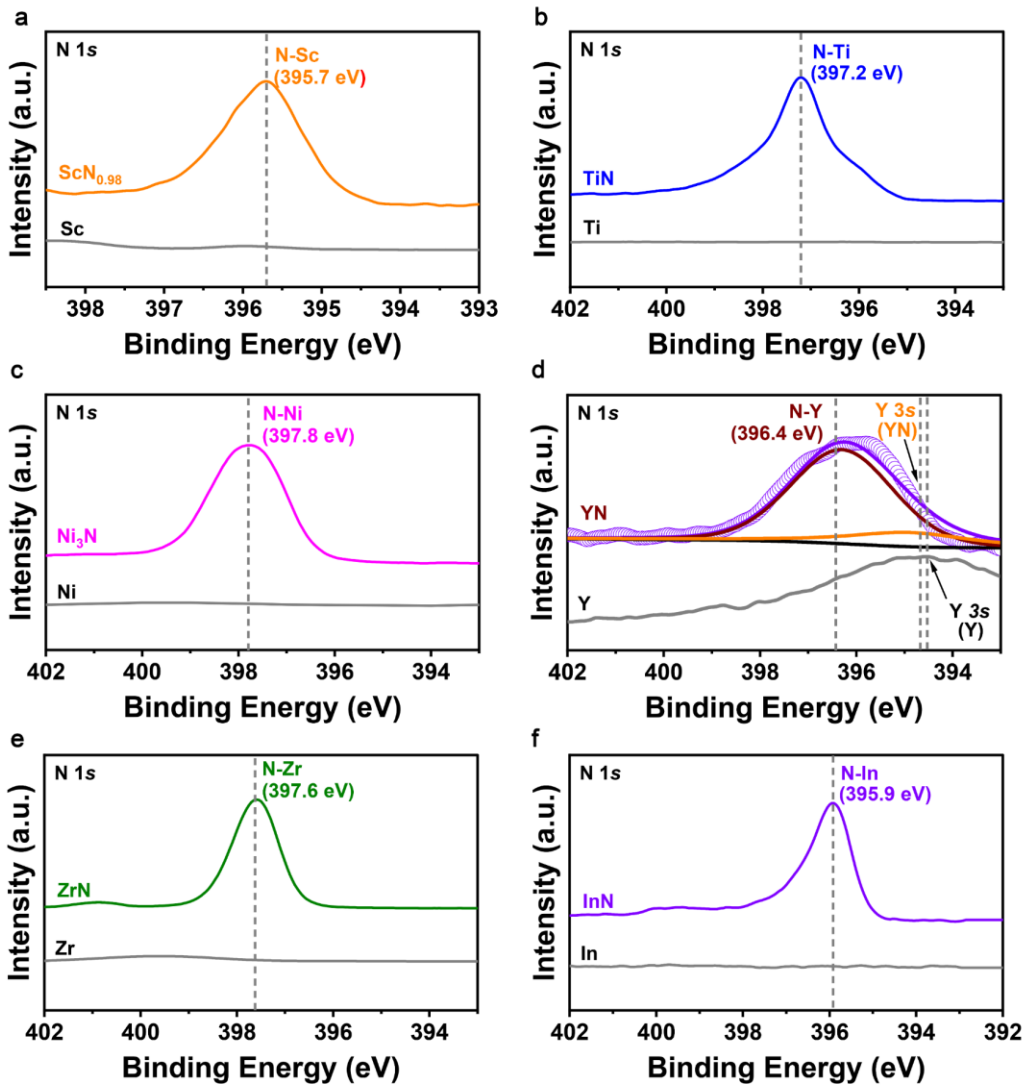

Supplementary Figure 6. X-ray photoelectron spectroscopy (XPS) spectra. a-f, The N 1*s* XPS spectra of different metal nitrides synthesized from respective metal precursors, including $ScN_{0.98}$ (**a**), TiN (**b**), Ni_3N (**c**), YN (**d**), ZrN (**e**) and InN (**f**). **a,** The N 1*s* peak at 395.7 eV of $ScN_{0.98}$ was assigned to the N-Sc bond[5]. **b,** The TiN sample show that the N 1*s* signal appears at 397.2 eV, which originated from the N-Ti contribution[6]. **c,** The N 1*s* peak at 397.8 eV is associated to the binding energy of N-Ni in Ni_3N structure[7]. **d,** The XPS spectrum of YN show two peaks that located at 396.4 eV and 394.7 eV, corresponding to N 1*s* signal of the N-Y bonds and Y 3*s* in the YN structure, respectively[8]. Moreover, Y metal also exhibits a Y 3*s* peak at the 394.6 eV[8]. **e,** The N 1*s* spectra of ZrN show a peak related to the N-Zr bond at 397.6 eV[9]. **f,** The InN sample show that the N 1*s* signal appears at 395.9 eV, which is assigned to the N-In bond of the InN structure[10].

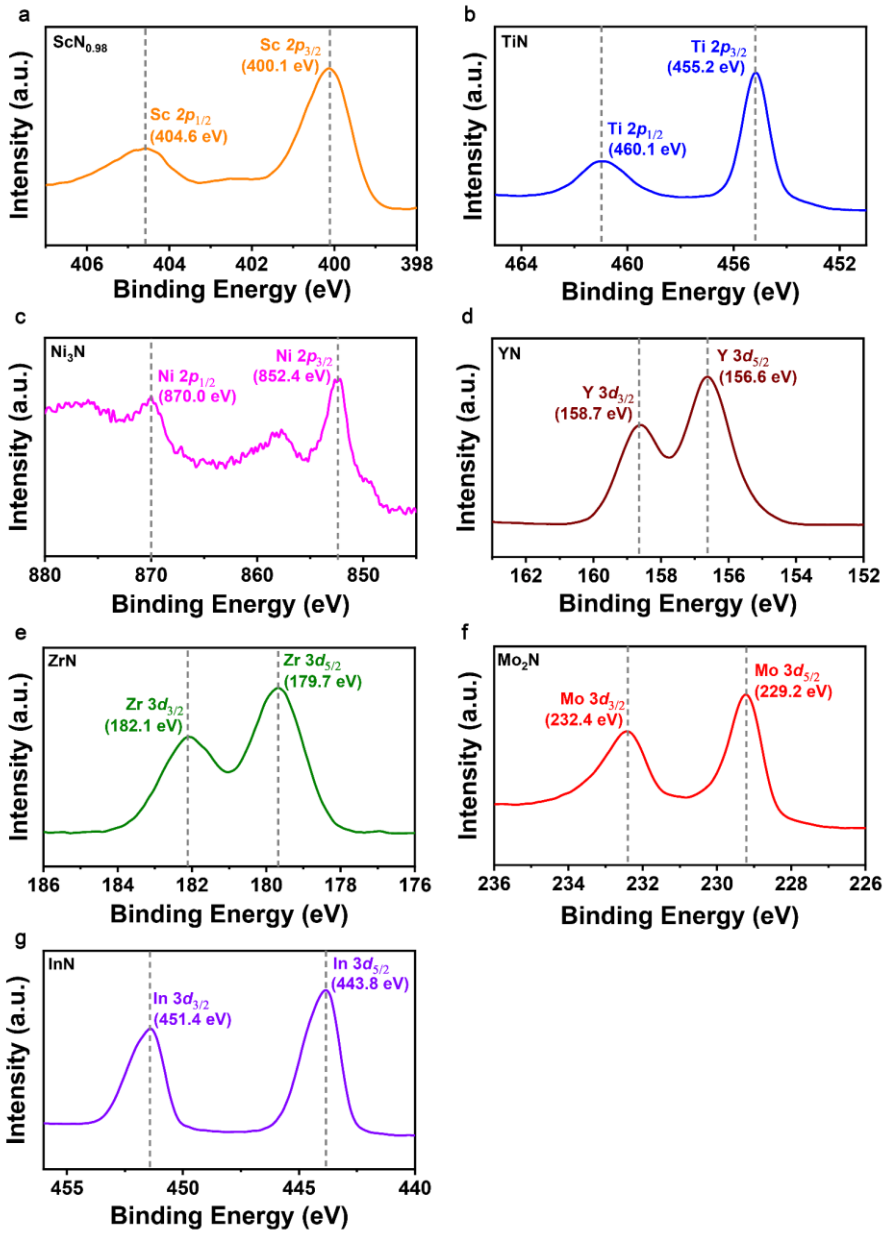

Supplementary Figure 7. XPS spectra. a-g, The metal XPS spectra of different metal nitrides synthesized from respective metal precursors, including $ScN_{0.98}$ (**a**), TiN (**b**), Ni_3N (**c**), YN (**d**), ZrN (**e**), Mo_2N (**f**) and InN (**g**). **a,** The Sc $2p_{3/2}$ peak at 400.1 eV and Sc $2p_{1/2}$ peak at 404.6 eV of $ScN_{0.98}$ were assigned to the N-Sc bond[5]. **b,** The TiN sample show that the Ti $2p_{3/2}$ and Ti $2p_{1/2}$ signals appear at 455.2 eV and 460.1 eV, which originated from the N-Ti contribution[6]. **c,** The Ni $2p_{3/2}$ and Ni $2p_{1/2}$ peak at 852.4 eV and 870.0 eV are associated to the binding energy of N-Ni in Ni_3N structure[7]. **d,** The XPS spectrum of YN show two peaks that located at 156.6 eV and 158.7 eV, corresponding to Y $3d_{5/2}$ and Y $3d_{3/2}$ signal of the N-Y bonds, respectively[8]. **e,** The Zr $3d$ spectra of ZrN show two peaks related to the N-Zr bond at 179.9 eV and 182.1 eV[11]. **f,** The Mo_2N sample show that the Mo $3d_{5/2}$ and Mo $3d_{3/2}$ signals appear at 229.2 eV and 232.4 eV, which originated from the N-Mo contribution[1]. **g,** The InN sample show that the In $3d_{5/2}$ and In $3d_{3/2}$ signals appear at 443.8 eV and 451.4 eV, which were assigned to the N-In bond of the InN structure[10].

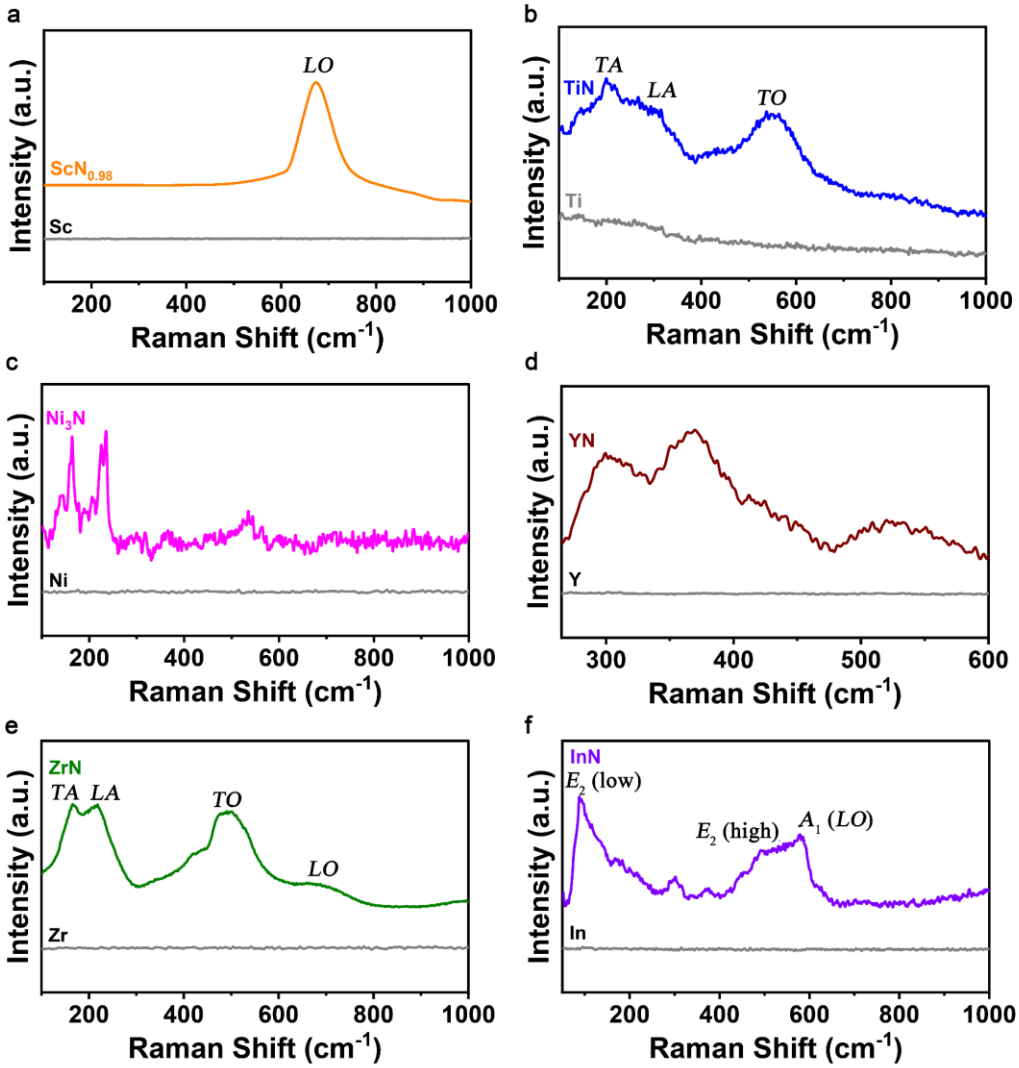

Supplementary Figure 8. Raman spectra. a-f, The Raman spectrum of different metal nitrides synthesized from respective metal precursors, including $ScN_{0.98}$ (**a**), TiN (**b**), Ni_3N (**c**), YN (**d**), ZrN (**e**) and InN (**f**). **a,** The $ScN_{0.98}$ shows a Raman peak at 674 cm^{-1}, corresponding to the longitudinal optical (*LO*) phonon mode[12]. **b,** The Raman spectra of TiN show peaks at 203 cm^{-1}, 298 cm^{-1}, and 552 cm^{-1}, which correspond to the transverse acoustic (*TA*), longitudinal acoustic (*LA*), and transverse optical (*TO*) phonon modes, respectively[13]. The scattering in the acoustic range (*TA* and *LA* modes) is primarily determined by vibrations of the Ti ions, while the scattering in the optical range (*TO* mode) is owing to vibrations of the N ions[14]. **c,** The Ni_3N exhibits the characteristic peaks at 158 cm^{-1}, 222 cm^{-1}, and 510 cm^{-1}, which are typical Ni_3N Raman peaks, in consistent with literature results[15, 16]. **d,** The Raman peaks of YN at 301 cm^{-1} and 369 cm^{-1} could be attributed to acoustic phonons in cubic YN. And the broad peak with lower intensity at 528 cm^{-1} most probably originated from optical phonons[17]. **e,** The Raman spectra of ZrN exhibits two peaks at 162 cm^{-1} and 217 cm^{-1}, corresponding to the *TA* and *LA* transition modes, respectively. In addition, two more peaks at higher frequencies (495 cm^{-1}, and 684 cm^{-1}) can be attributed to *TO* and *LO* transition modes, respectively[18, 19]. **f,** Raman spectra of InN show distinct peaks at the 94 cm^{-1}, 492 cm^{-1} and 580 cm^{-1}, which correspond to the E_2 (low), E_2 (high) and *LO* phonon modes of InN, respectively[20].

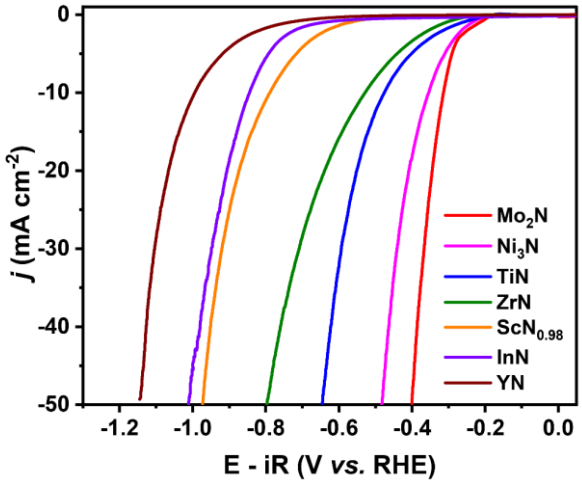

Supplementary Figure 9. HER polarization curves. HER polarization curves of different metal nitrides in natural seawater, including $ScN_{0.98}$, TiN, Ni_3N, YN, ZrN, Mo_2N, and InN (100% iR correction, where R was determined to be 23.7 ± 0.2 Ω). Catalyst loading: ~1.00 mg cm^{-2}. Sweep rate: 5 mV s^{-1}. Rotation rate: 1600 rpm. The HER activity increases in the order of YN < InN < $ScN_{0.98}$< ZrN < TiN < Ni_3N < Mo_2N.

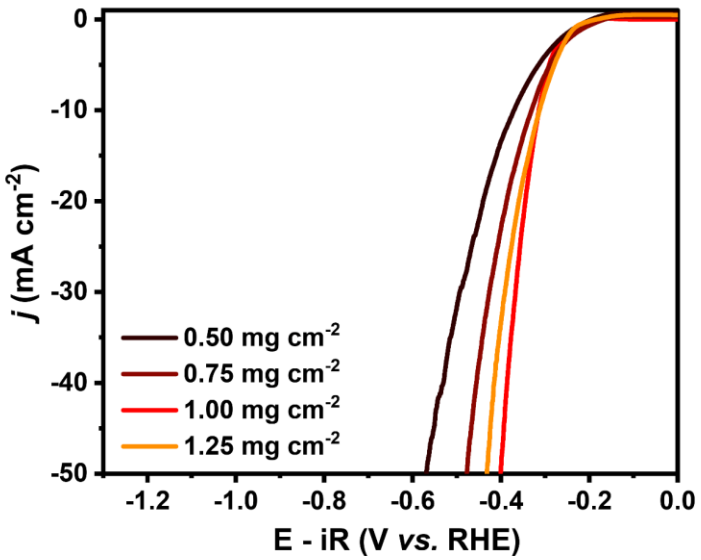

Supplementary Figure 10. The effect of catalyst loadings on HER. We measure the HER polarization curves of Mo_2N with different loadings from 0.50 mg cm^{-2} to 1.25 mg cm^{-2} in Ar-saturated natural seawater (100% iR correction, where R was determined to be 23.7 ± 0.2 Ω). Sweep rate: 5 mV s^{-1}. Rotation speed: 1600 rpm. It can be seen that the current increases as the catalyst loading increases until the loading arrives at 1.00 mg cm^{-2}. Further increasing the loading leads to a decreased activity. The optimized catalyst loading amount of Mo_2N catalyst was 1 mg cm^{-2} and this value was fixed for all the relevant electrochemical tests.

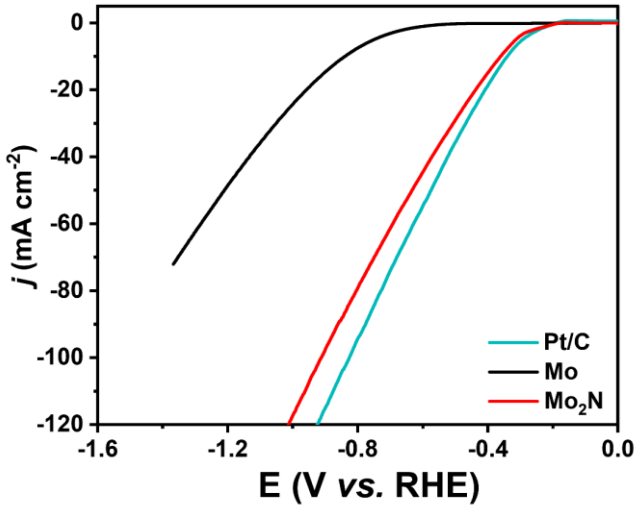

Supplementary Figure 11. HER polarization curves. HER polarization curves of Mo, Mo_2N, and commercial Pt/C catalysts in natural seawater on a 0.196 cm^2 electrode without iR correction (100% iR correction, where R was determined to be 23.7 ± 0.2 Ω). Catalyst loading: ~1.0 mg cm^{-2}. Sweep rate: 5 mV s^{-1}

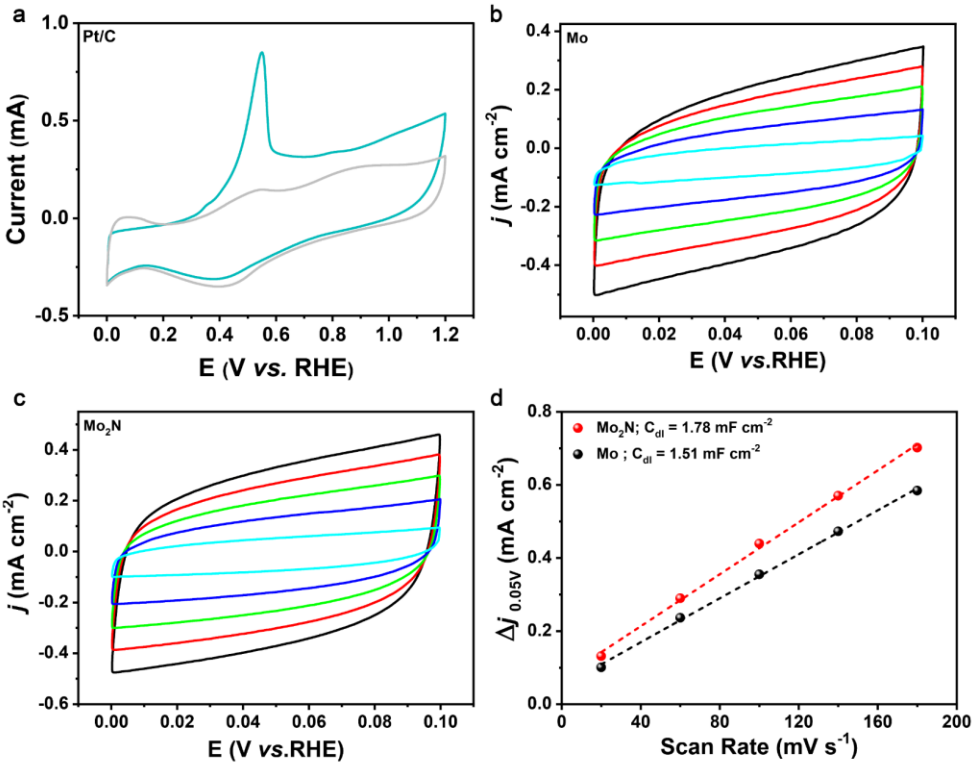

e

Catalyst	ECSA (cm^2)
Pt/C	21.43
Mo	9.87
Mo_2N	11.63

Supplementary Figure 12. Estimation of ECSA. a, The CO stripping curves for Pt/C. The gray curves showed the second cycle of the measurements. Sweep rate: 20 mV s^{-1}. Rotation speed: 1600 rpm. **b, c,** CV in the region of 0.0~0.1 V versus RHE for Mo and Mo_2N catalysts at the following scan rate: (cyan line) 20, (blue line) 60, (green line) 100, (red line) 140, and (black line) 180 mV/s. **d,** Plots showing the extraction of the C_{dl} for Mo and Mo_2N catalysts. **e,** Summary of the ECSA of different catalysts.

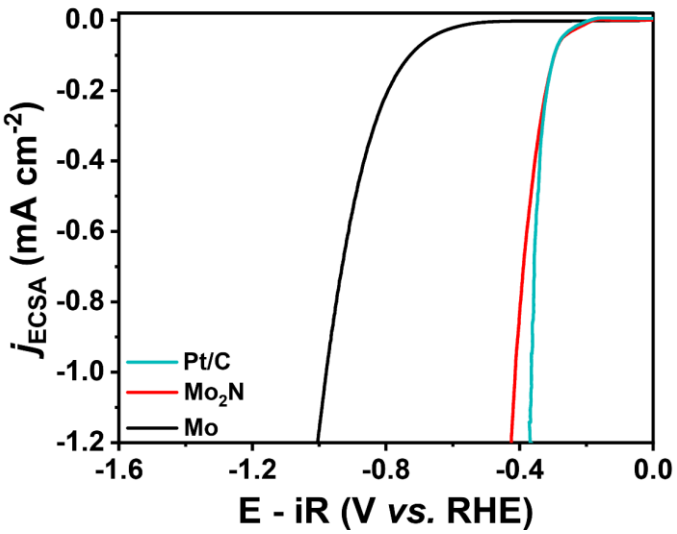

Supplementary Figure 13. HER polarization curves. ECSA-normalized HER polarization curves of Mo, Mo_2N, and commercial Pt/C catalysts measured in natural seawater (100% iR correction, where R was determined to be 23.7 ± 0.2 Ω). Catalyst loading: ~1.0 mg cm^{-2}. Sweep rate: 5 mV s^{-1}.

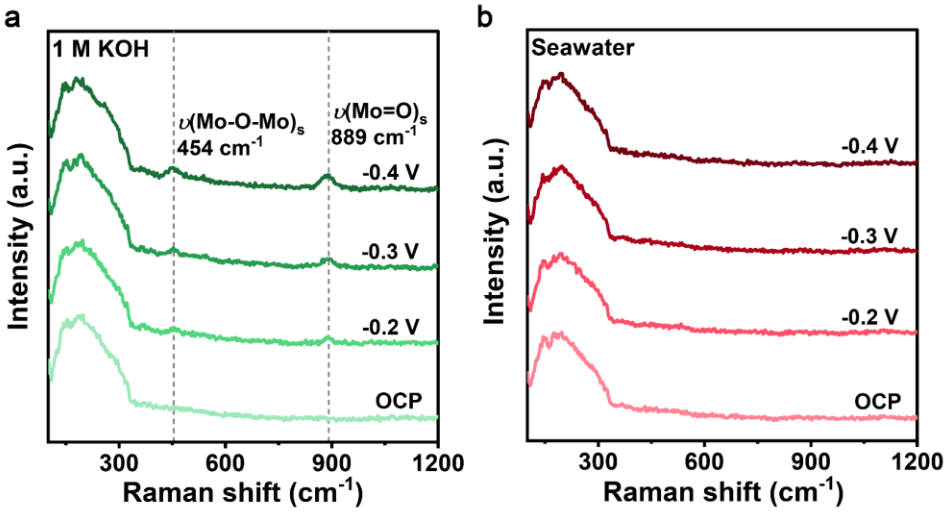

Supplementary Figure 14. In situ Raman spectra. a, b, Potential-dependent in situ Raman spectra of Mo_2N during HER process in 1 M KOH (**a**) and natural seawater (**b**). In 1 M KOH, the in situ Raman spectra show that two peaks at 454 cm^{-1} and 889 cm^{-1} arise and grow gradually when negative potentials progressively applied. Such two peaks can be assigned to the symmetric stretching mode of Mo-O-Mo and Mo=O, respectively[21, 22], showing the formation of MoO_4^{2-} on the Mo_2N surface in alkali. By contrast, in natural seawater, no MoO_x signals can be detected on the Mo_2N surface at all potentials examined.

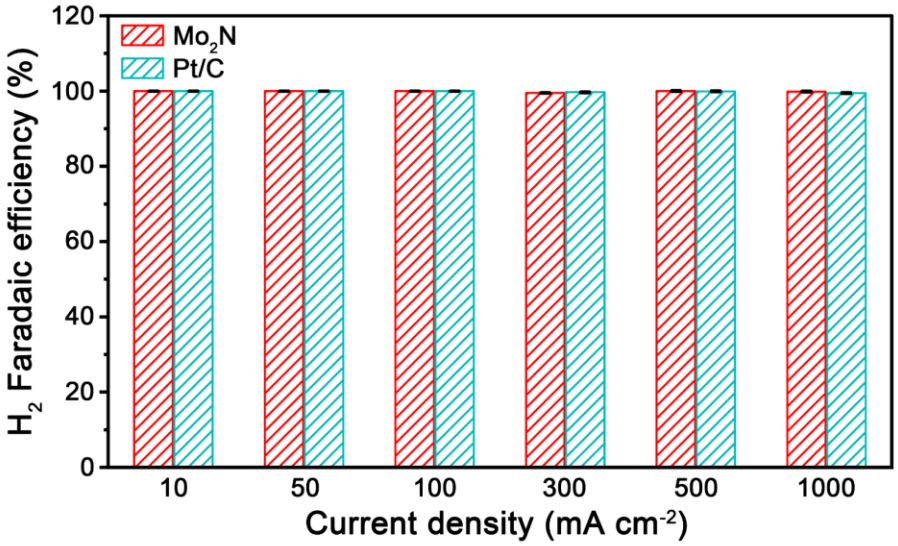

Supplementary Figure 15. Faradaic efficiency. H_2 Faradaic efficiencies of the Mo_2N and Pt/C catalyst at different current densities. Error bars are based on the standard deviation of three independent measurements. The measured H_2 gas at all current densities perfectly match with the theoretical values, corresponding to Faradaic efficiency of ~100%

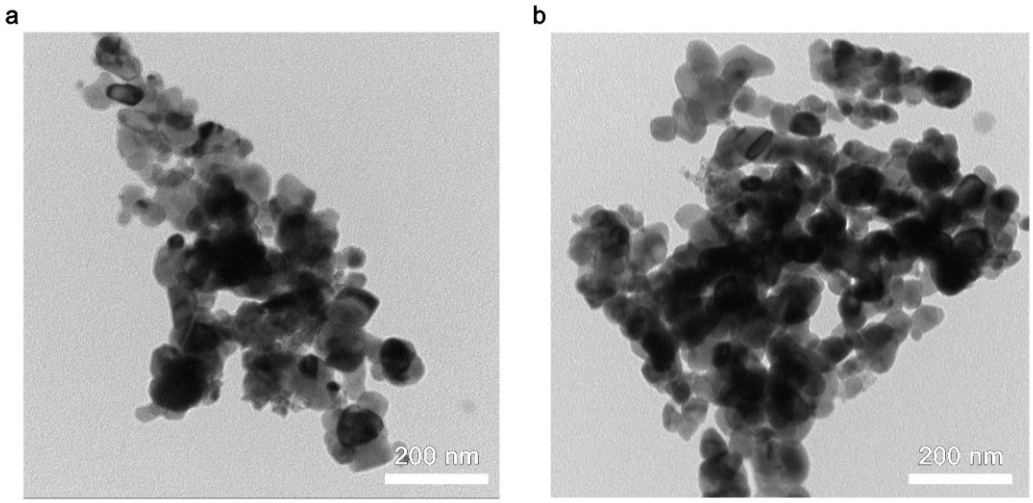

Supplementary Figure 16. TEM characterization. a, b, TEM characterization of the Mo_2N catalyst after 1,000 h operation. The TEM results reveal that the Mo_2N catalyst can retain their original morphology after stability test.

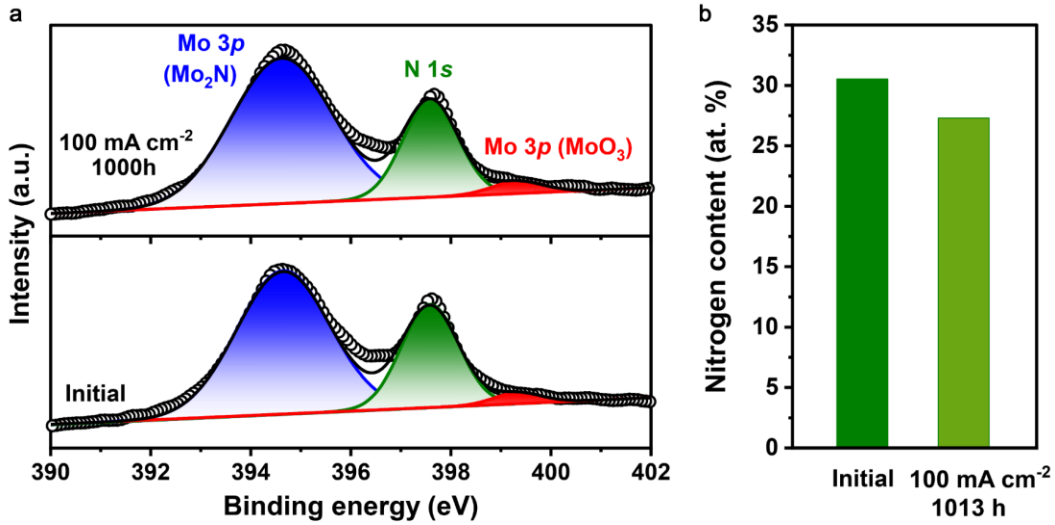

Supplementary Figure 17. Stability of Mo_2N. a, b, The Mo 3*p*, N 1*s* (**a**) and corresponding N content (**b**) of the Mo_2N catalyst before and after HER. The results show that the valence states and surface structure of both Mo and N were well maintained over 1,000 hours of operation.

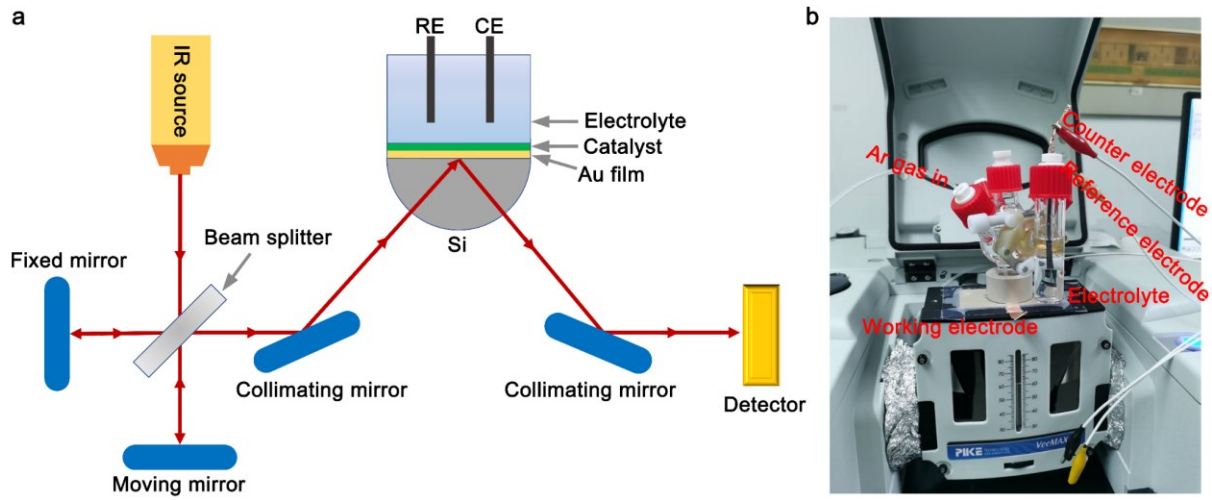

Supplementary Figure 18. In situ SEIRAS measurements. a, Schematic of the set-up for in situ SEIRAS measurements. **b**, Photograph of the set-up for in situ SEIRAS measurements.

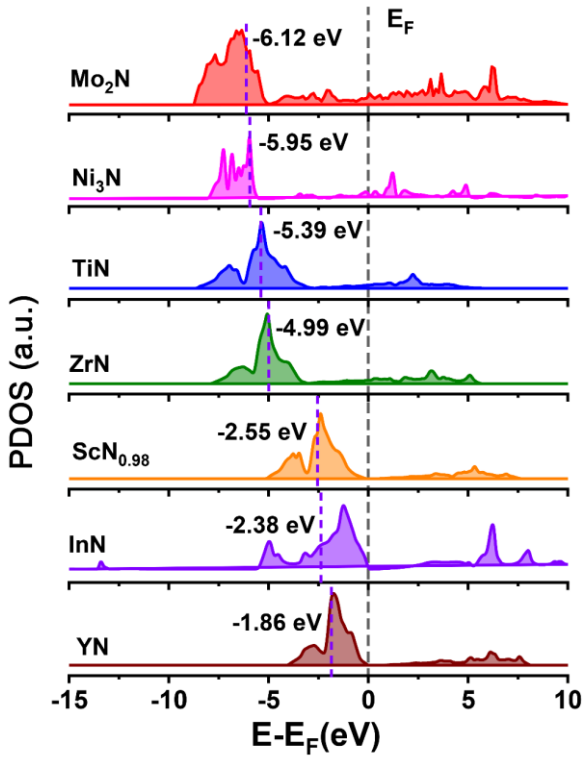

Supplementary Figure 19. Partial density of states (PDOS). Calculated PDOS of N 2*p* orbital in each metal nitride with the Fermi level (E_F) aligned at 0 eV. The 2*p* band centers of the N elements are marked by the purple dotted lines, deviating from the Fermi level in the order of YN < InN < $ScN_{0.98}$< ZrN < TiN < Ni_3N < Mo_2N.

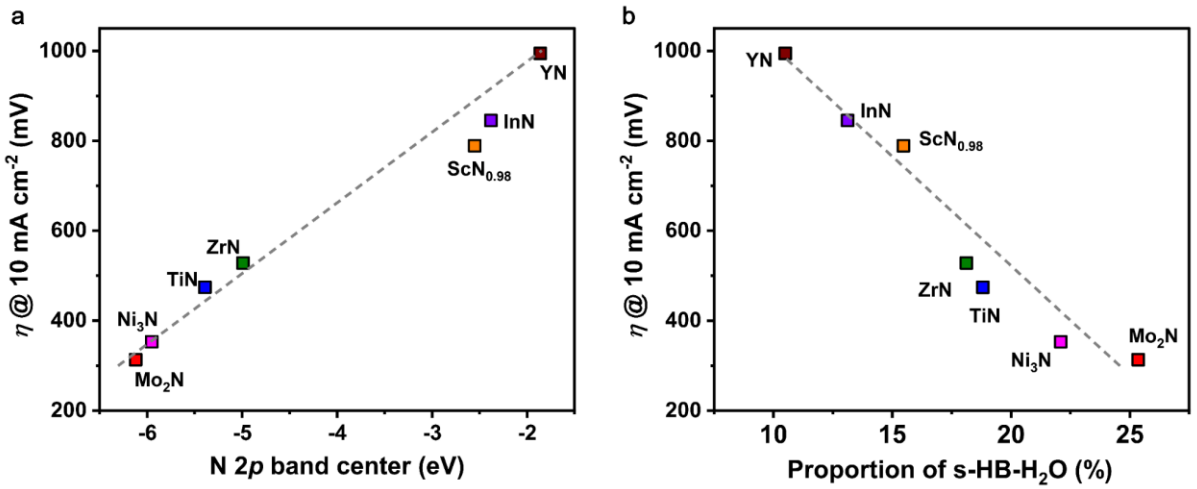

Supplementary Figure 20. Electrocatalytic HER Performances of metal nitrides. a, b, HER activity as a function of N 2*p* band center of each metal nitride (**a**) and proportion of strongly H-bonded H_2O molecules in the EDL of each metal nitride (**b**). The HER activity exhibits a linear dependence on the N 2*p* band center and proportion of strongly H-bonded H_2O molecules in the EDL of each metal nitride.

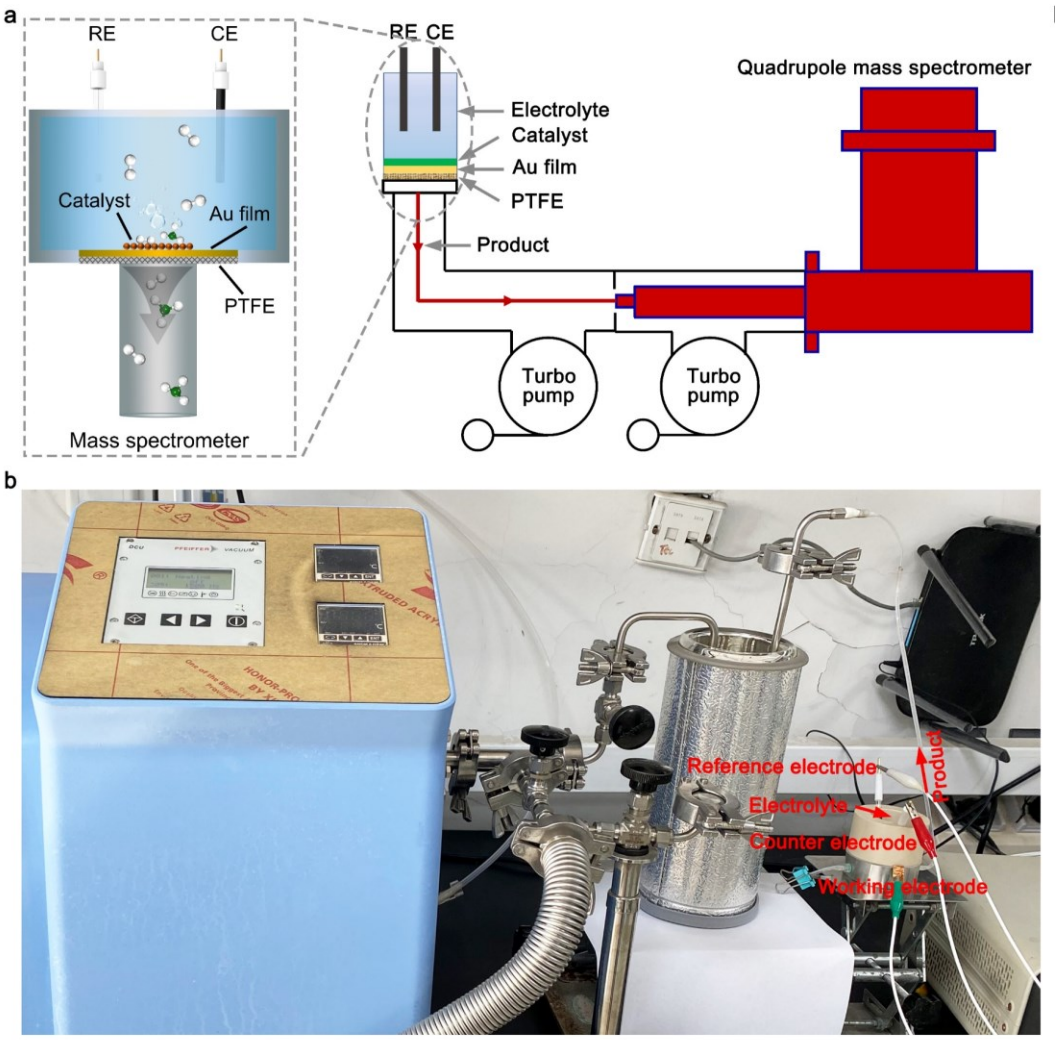

Supplementary Figure 21. In situ DEMS measurements. a, Schematic of the set-up for in situ DEMS measurements. **b,** Photograph of the set-up for in situ DEMS measurements.

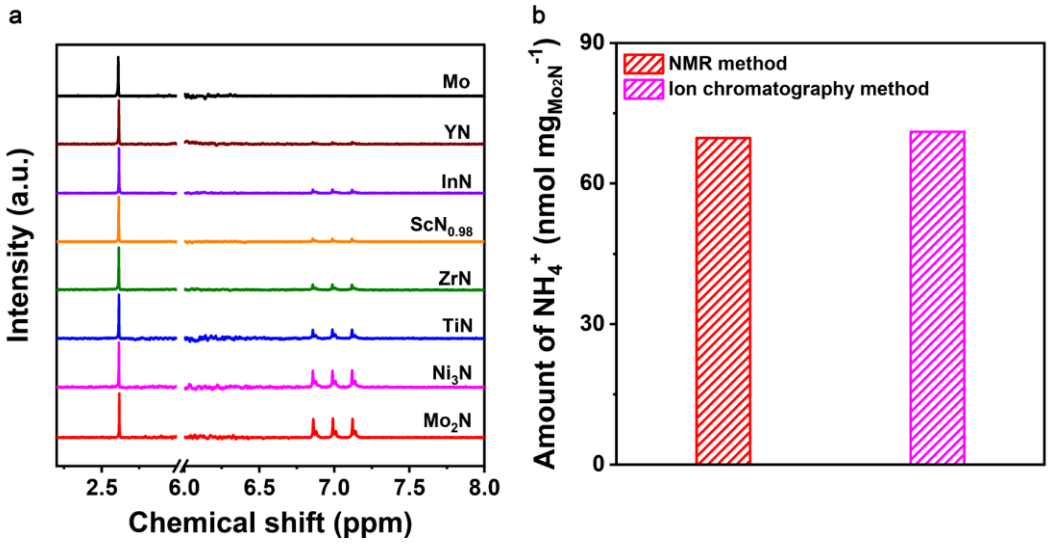

Supplementary Figure 22. NMR measurement. a, ^{1}H NMR spectra of the NH_4^+ generated during the electrocatalytic HER with metal nitrides as catalysts in natural seawater at -10 mA cm^{-2}. **b,** The amount of NH_4^+ generated with Mo_2N as catalysts in natural seawater at -10 mA cm^{-2} using different quantification methods. The ^{1}H NMR spectra show a pronounced triplet in the region of 6.8-7.15 ppm for Mo_2N, showing that NH_4^+ forms during HER and exists in our system[23]. For other metal nitrides, such triplet from NH_4^+ were also observed but with gradually weaker strength. By contrast, no NH_4^+ can be detected in the control experiment using Mo as the catalyst (**a**), confirming that the obtained NH_4^+ comes from the lattice nitrogen. The amount of NH_4^+ formed on Mo_2N detected by ion chromatography method agrees well with the data obtained by the quantitative ^{1}H NMR method.

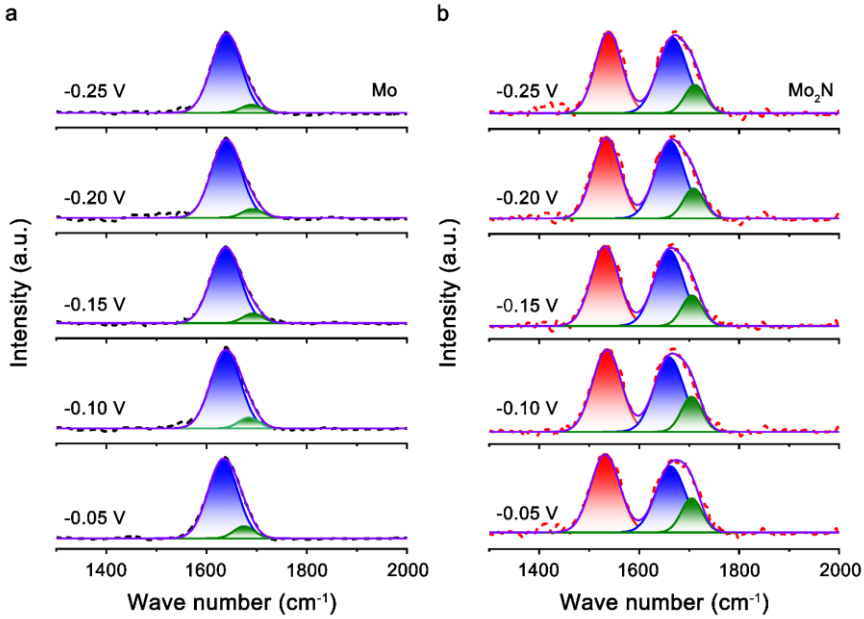

Supplementary Figure 23. In situ SEIRAS spectra. a, b, The in situ SEIRAS spectra recorded at potentials from -0.05 to -0.25 V versus RHE on Mo (**a**) and Mo_2N (**b**) in Ar-saturated natural seawater.

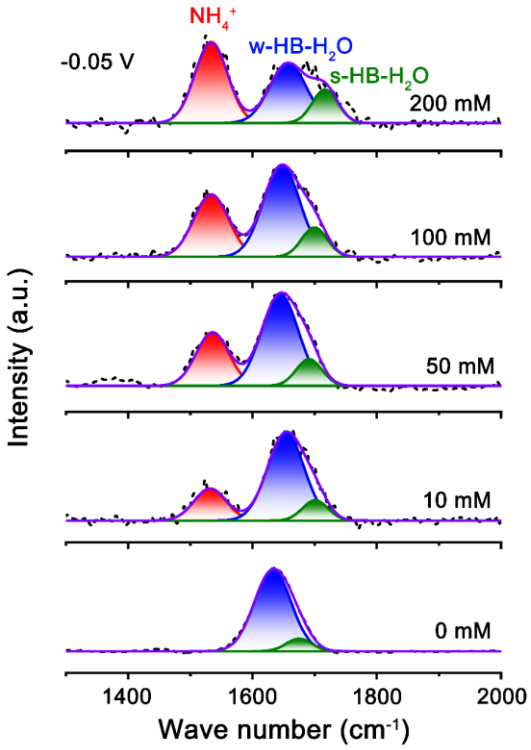

Supplementary Figure 24. In situ SEIRAS spectra. The in situ SEIRAS spectra recorded at -0.05 V versus RHE on Mo catalyst in Ar-saturated natural seawater with different concentration of NH_4Cl. The pH of the bulk seawater was fixed at 7.84 by NaOH.

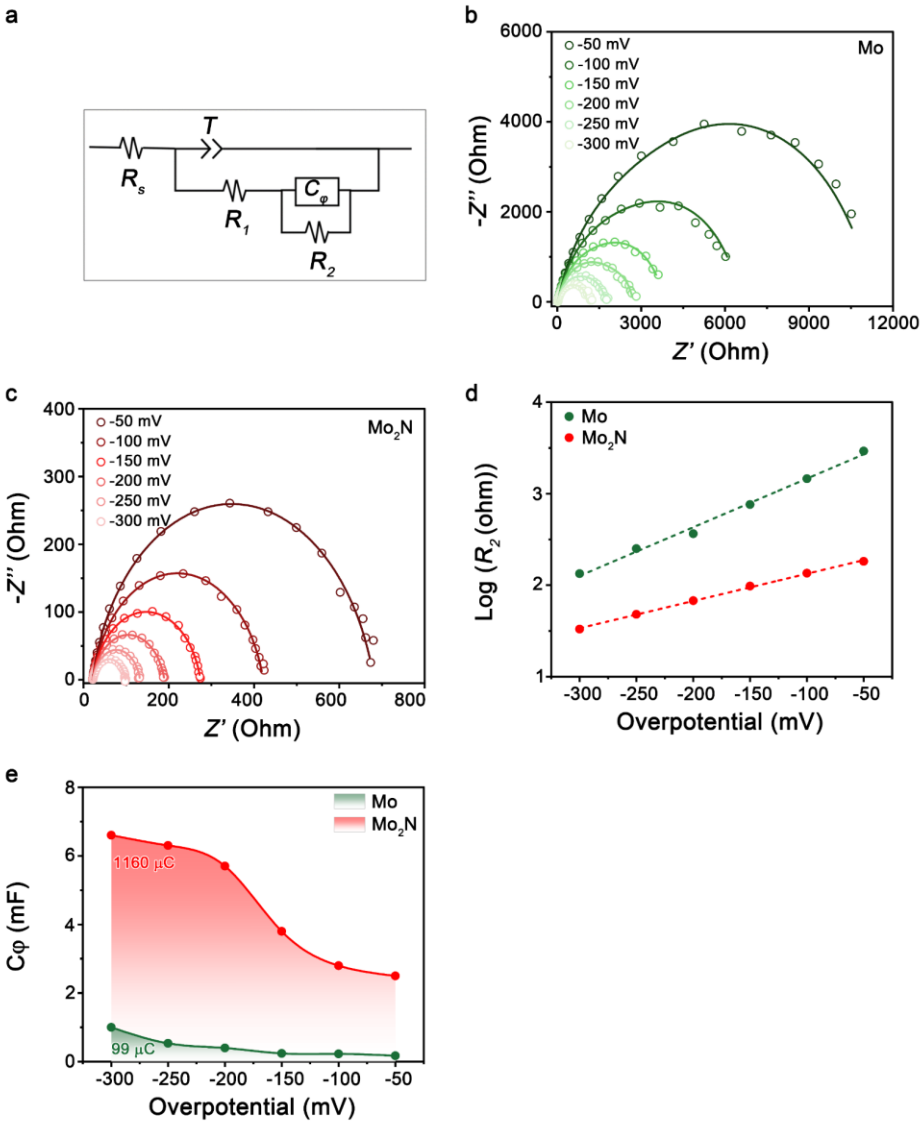

Supplementary Figure 25. EIS Nyquist plots. a, The equivalent circuit for the EIS simulation. R_s represents the solution resistance. T and R_1 represent the double layer capacitance and the catalytic charge transfer resistance, respectively. C_φ and R_2 are the hydrogen adsorption pseudo-capacitance and resistance, respectively. **b, c,** The EIS Nyquist plots of Mo (**b**) and Mo_2N (**c**) were measured at different overpotentials in Ar-saturated natural seawater. Solid lines are the fitting results according to the equivalent circuit. **d,** EIS-derived Tafel plots of the Mo and Mo_2N obtained from the hydrogen adsorption resistance R_2. **e.** Plots of C_φ vs. η of the bare Mo and Mo_2N catalysts during HER in Ar-saturated natural seawater. The EIS-derived Tafel plots (**d**) show that Mo_2N has a much lower hydrogen adsorption resistance than Mo at all overpotential examined, indicating its faster hydrogen adsorption and transfer kinetics. Moreover, the integration of C_φ versus η profiles (**e**) provides information on the hydrogen adsorption charge (Q_H) on the catalyst surface during HER[24, 25]. The results show an increased amount of adsorbed hydrogen on Mo_2N ($Q_H[Mo_2N]$ = 1160 μC) compared with that of Mo (Q_H[Mo] = 99 μC), implying that NH_4^+ species in the Stern layer on Mo_2N surface greatly improve the hydrogen adsorption.

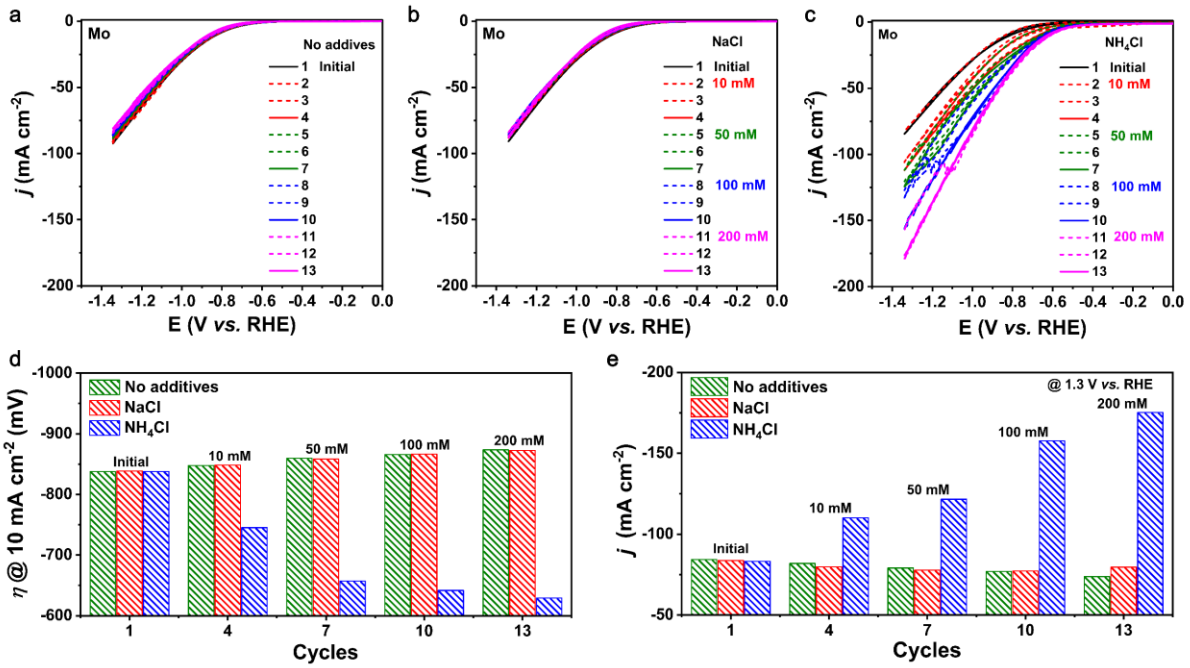

Supplementary Figure 26. Polarization curves of Mo in the natural seawater. a, The HER polarization curves of Mo in the natural seawater. **b, c,** The HER polarization curves of Mo in the natural seawater with different concentration of NaCl (**b**) and NH_4Cl (**c**). **d, e,** The corresponding overpotential at 10 mA cm^{-2} (**d**) and current density at 1.3 V versus RHE (**e**). All the polarization curves were not corrected with iR compensation and the pH of the bulk seawater was fixed at 7.84 by adding NaOH. The results reveal that the HER activity of Mo catalyst improves as the concentration of NH_4^+ increases.

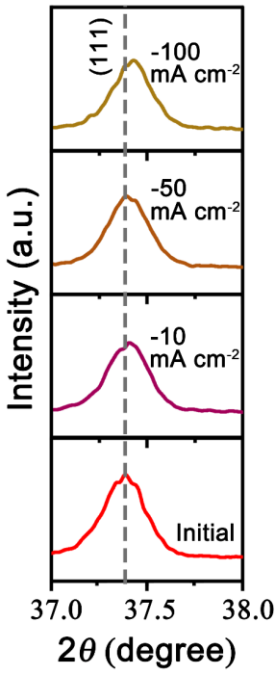

Supplementary Figure 27. The enlarged XRD patterns. The enlarged XRD patterns of Mo_2N catalysts after electrolysis at different current densities for 36 hours in natural seawater. The XRD peak corresponding to the Mo_2N (111) facets shifted gradually to higher angles as the current density increases, indicative of an increase of N vacancies[26].

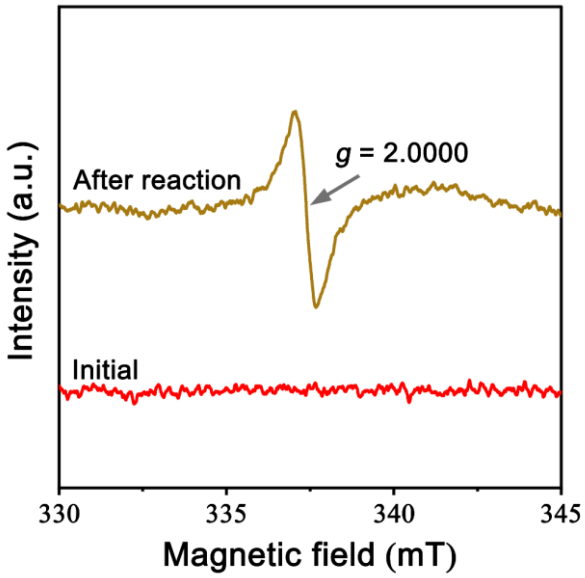

Supplementary Figure 28. EPR spectra. EPR spectra of Mo_2N before and after electrolysis at -100 mA cm^{-2} for 36 hours in natural seawater. The results show a strong EPR signal at a *g* value of 2.0000 for the Mo_2N catalyst after electrolysis at -100 mA cm^{-2} for 36 h in natural seawater, confirming the formation of N vacancies[27].

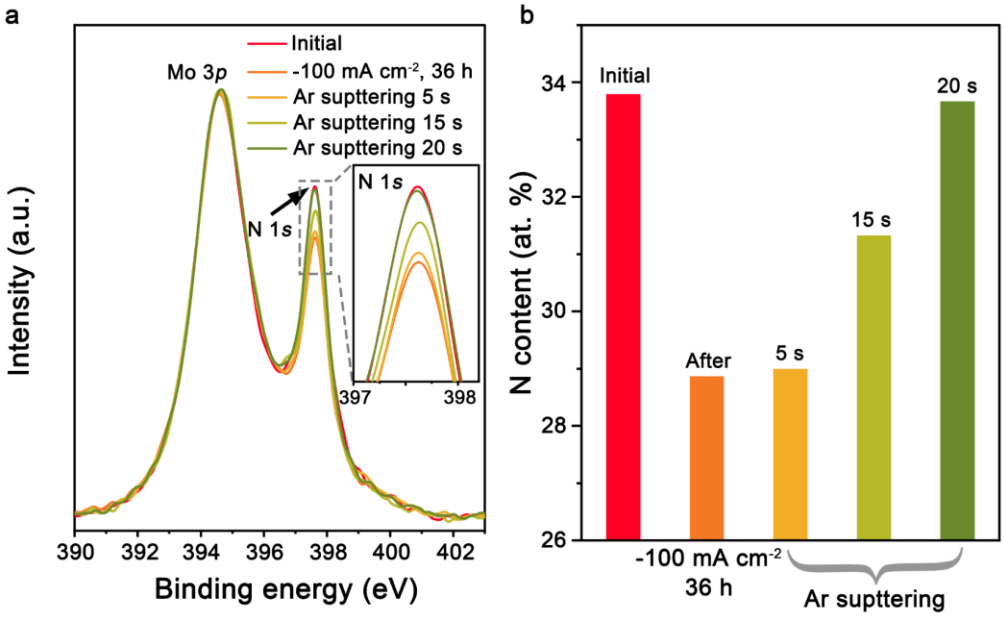

Supplementary Figure 29. XPS depth measurements. a, b, the N 1*s* XPS spectra of the Mo_2N before and after electrolysis at -100 mA cm^{-2} for 36 hours in natural seawater and after different Ar sputtering time (5s, 15s and 20s) (**a**) and the corresponding N content (**b**). The results show that the N content increases with the depth of detection until approaching the initial nitrogen content of Mo_2N, which indicates that the lattice nitrogen on the Mo_2N surface makes NH_4^+, rather than the lattice N from the deep structure.

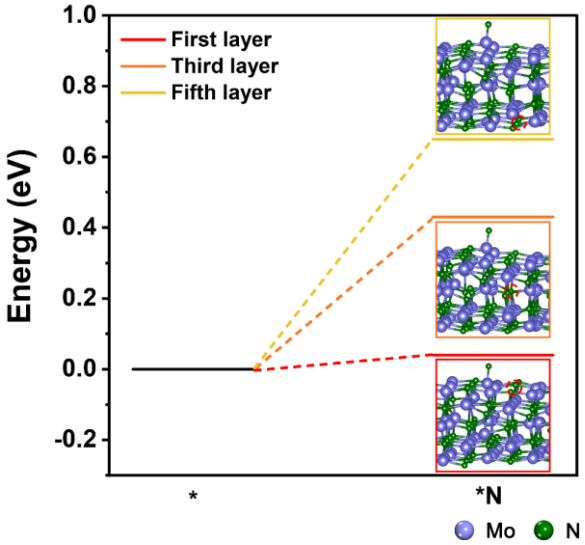

Supplementary Figure 30. DFT calculations. Free energy diagram of lattice nitrogen in different atomic layer of Mo_2N transfers to the surface metal site, including first, third and fifth layer. Insets show corresponding structure models. The DFT calculations predict that the energy barriers required for the migration of N from the first, third, and fifth layers of Mo_2N to the surface Mo atoms could be 0.04 eV, 0.43 eV and 0.65 eV, respectively.

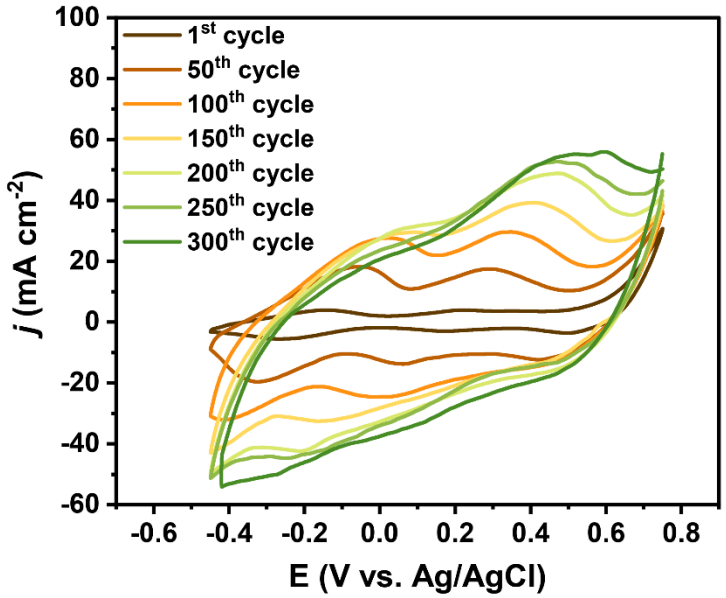

Supplementary Figure 31. IrO_x deposition. The CV curves obtained for IrO_x deposition on Pt-ring electrode with a scan rate of 1 V s^{-1}.

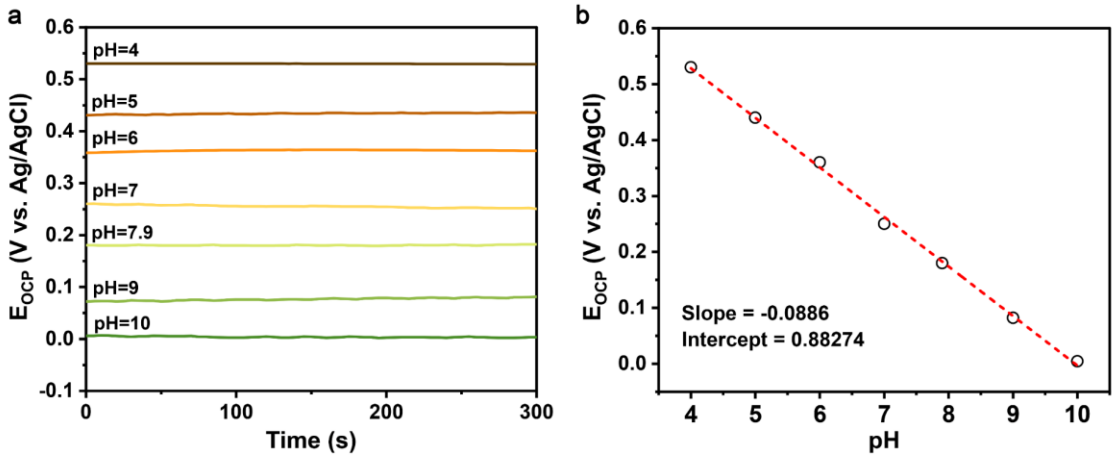

Supplementary Figure 32. pH measurement on catalyst surface. a, b, The time (**a**) and pH (**b**) dependence of open circuit potential (E_{ocp}) for IrO_x electrodeposited Pt-ring electrode. The measurement was performed in natural seawater. The pH of the bulk seawater was adjusted by adding H_2SO_4 or NaOH.

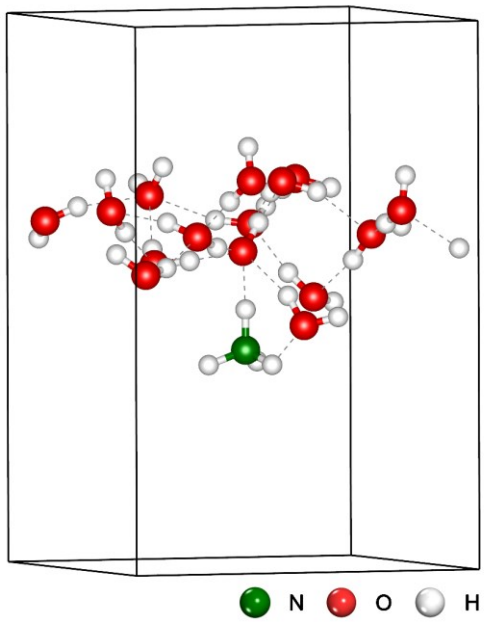

Supplementary Figure 33. Density functional theory (DFT) simulations. Optimized structures of NH_4^+ surrounded by OH^- and H_2O molecules. We fixed the NH_4^+ as it was confined on the catalyst surface via a strong electric field. And the OH^- and H_2O molecules were allowed to fully relax. When the structure reached required accuracy, the OH^- and H_2O molecules are interacting strongly with the hydrogen of the NH_4^+ through H-bond.

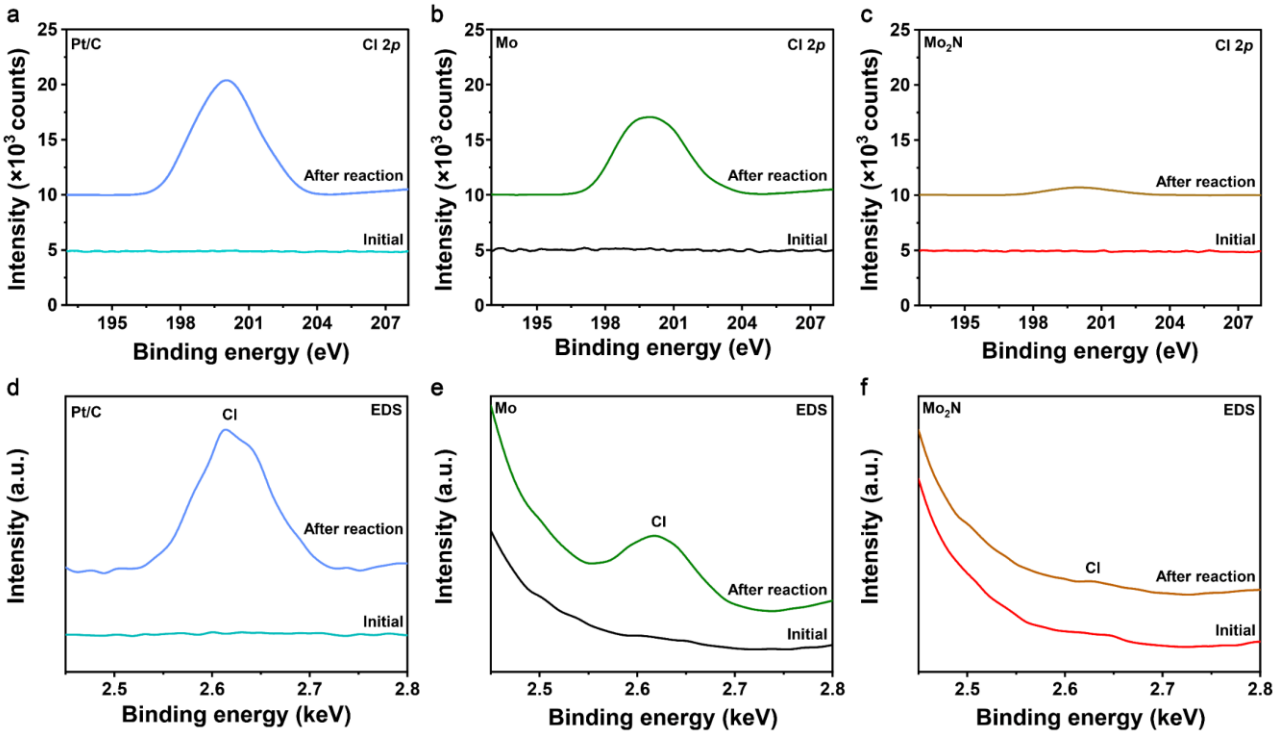

g

Sample	Element content (at.%)			
	Pt	Mo	N	Cl
Pt/C	71.23	\	\	28.77
Mo	\	90.72	\	9.28
Mo_2N	\	72.11	27.75	0.15

Supplementary Figure 34. Cl resistance measurements. a-c, Cl 2*p* XPS spectra of Pt/C (**a**), Mo (**b**) and Mo_2N (**c**) catalysts before and after electrolysis at -100 mA cm^{-2} for 36 hours in natural seawater. **d-f,** EDS spectra of Pt/C (**d**), Mo (**e**) and Mo_2N (**f**) catalysts before and after electrolysis at -100 mA cm^{-2} for 36 hours in natural seawater. **g,** Summary of the atomic ratios of Pt/C, Mo and Mo_2N catalysts after electrolysis at -100 mA cm^{-2} for 36 hours in natural seawater based on EDS results. The results reveal that, after electrolysis at -100 mA cm^{-2} for 36 h in natural seawater, Pt-Cl component at 200.0 eV[28] (**a**) and Mo-Cl bond at 199.9 eV[29] (**b**) were detected for Pt/C and metallic Mo catalysts, respectively. By contrast, negligible XPS signal that belongs to Mo-Cl bond can be detected for Mo_2N catalyst after the same seawater electrolysis (**c**). Additionally, the EDS measurements show the same phenomenon (**d-f**). Based on the EDS results, the Cl contents can be determined to be about 28.77, 9.28 and 0.15 at. % on the surface of Pt/C, Mo and Mo_2N catalysts, respectively. These results together show that Mo_2N can resist Cl very well at the cathode during seawater electrolysis.

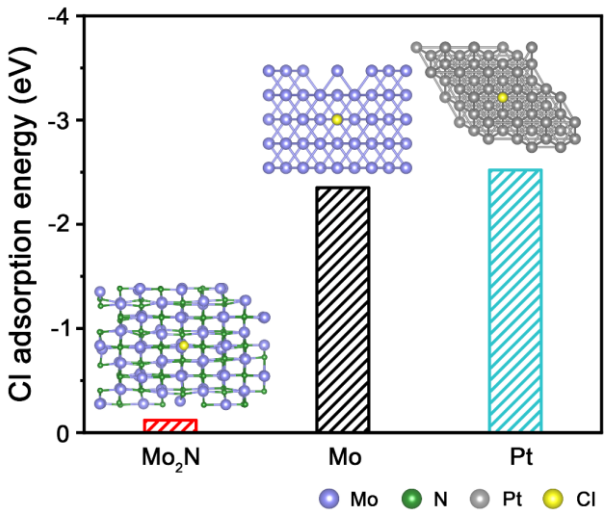

Supplementary Figure 35. DFT calculations. Cl adsorption energy of Mo_2N, Mo and Pt. Insets show corresponding structure models with Cl adsorption. Our calculations predict that Cl binding on Pt is strong, in agreement with previous report[30]. As to metallic Mo, the Cl binding ability is slightly weaker than Pt. By comparison, the Cl adsorption energy was found to be substantially weak on Mo_2N, which explains why no obvious Cl was detected on the Mo_2N catalyst.

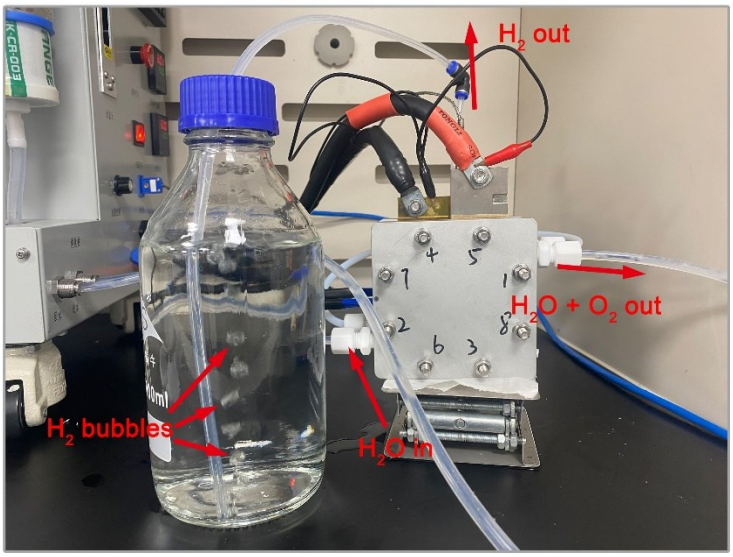

Supplementary Figure 36. Zero-gap membrane flow electrolyser. The photograph shows that the H_2 bubbles produced vigorously by the electrolyser with Mo_2N cathode.

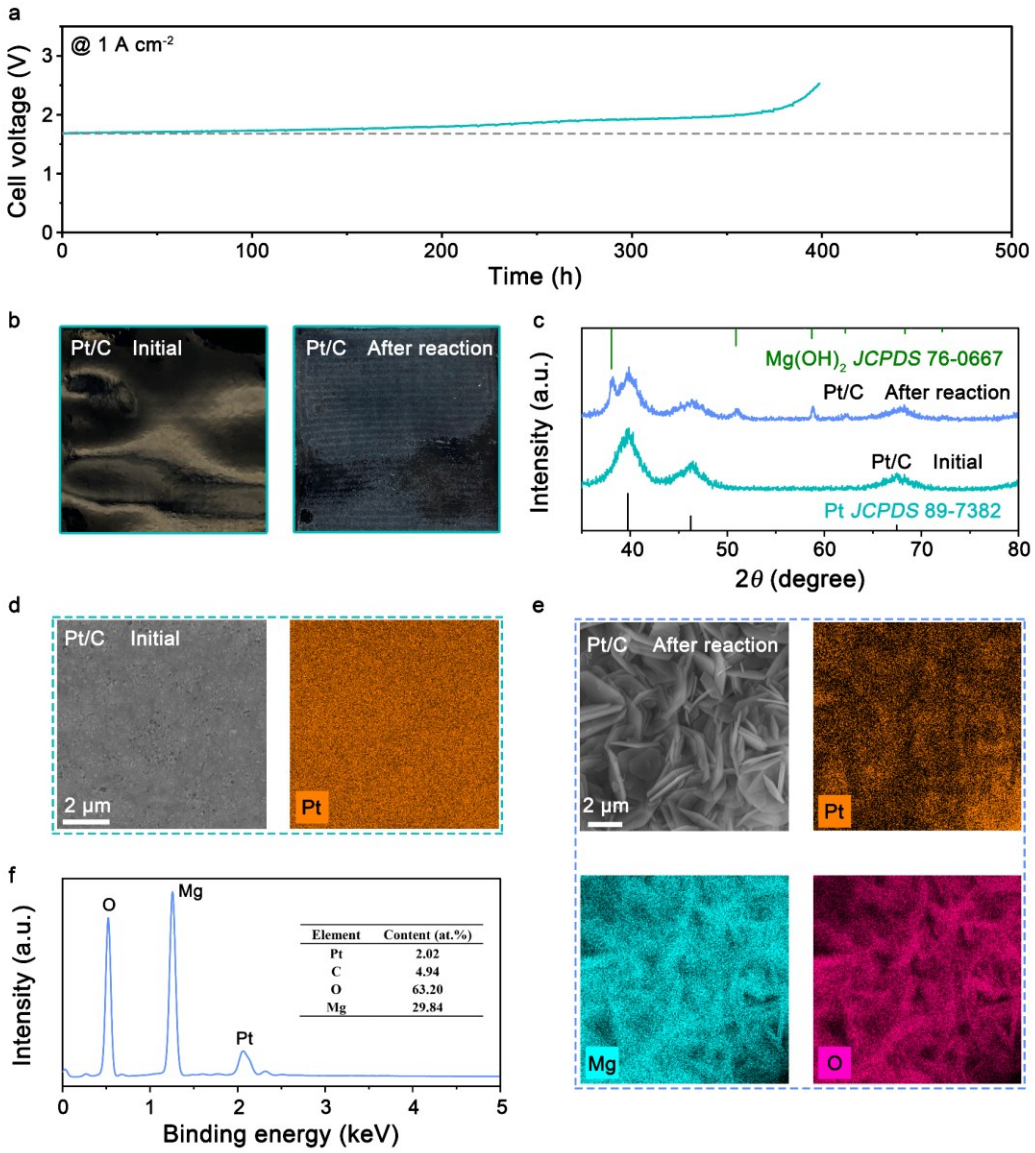

Supplementary Figure 37. Electrolyser performance. a, Chronopotentiometry measurement of the electrolyser at 1A cm^{-2} and 60 °C for Pt/C cathodic catalyst using simulated seawater as feed. **b, c,** Photographs (**b**) and XRD patterns (**c**) of Pt/C on Nafion 115 membrane before and after electrolysis at 1 A cm^{-2} for 399 hours. **d, e,** SEM image and its elemental mapping of Pt/C catalysts on Nafion 115 membrane before (**d**) and (**e**) after electrolysis at 1 A cm^{-2} for 399 hours. Scale bars: 2 μm. **f,** EDS spectra of Pt/C on Nafion 115 membrane after electrolysis at 1 A cm^{-2} for 399 hours. Inset shows corresponding atomic ratios. The results show that the device undergoes a rapid degradation with an apparent degradation rate of 2.16 mV h^{-1} (**a**). Photograph of the Pt/C electrode after 399-h test shows that some white precipitate forms (**b**). XRD patterns confirm that such white precipitate was mainly $Mg(OH)_2$ (**c**). Furthermore, SEM images show that flakelike $Mg(OH)_2$ forms on the Pt/C electrode (**d** and **e**). The corresponding element mapping exhibit a homogeneous distribution of Mg and O (**e** and **f**).

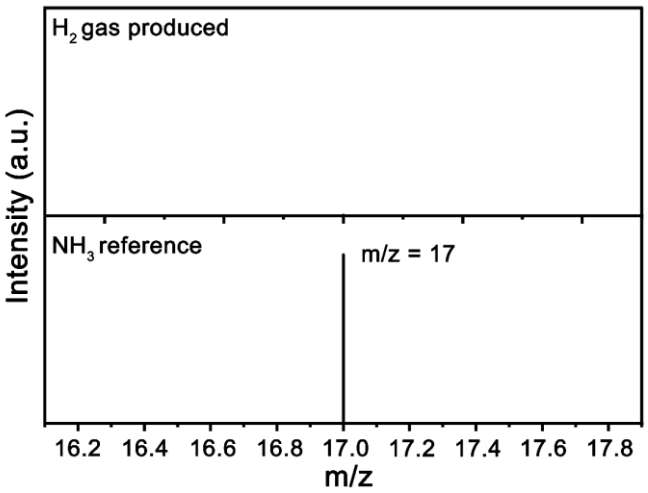

Supplementary Figure 38. GC-MS results. GC-MS spectra of NH_3 (down) and H_2 gas produced via the zero-gap membrane flow electrolyser with Mo_2N cathode at 1A cm^{-2} and 60 °C (top).

Supplementary Tables

Supplementary Table 1. Synthetic details and structural information of the nitrides synthesized from various metal powders.

Metal	Temperature (°C)	Nitride	*JCPDS*	Space Group	Structure
Sc	500	$ScN_{0.98}$	45-0978	Fm-3m	Cubic
Ti	400	TiN	38-1420	Fm-3m	Cubic
Ni	200	Ni_3N	10-0280	P6322	Hexagonal
Y	900	YN	35-0779	Fm-3m	Cubic
Zr	500	ZrN	65-9417	Fm-3m	Cubic
Mo	500	Mo_3N_2	25-1366	Pm-3m	Cubic
In	250	InN	50-1239	P63mc	Hexagonal

Supplementary Table 2. Structural parameters extracted from the Mo K-edge EXAFS fitting (S_0^2=0.90).

Sample	Scattering pair	CN	R(Å)	σ^2 (10^{-3} Å^2)	Δ E_0 (eV)	R factor
Mo	Mo-Mo1	8	2.72	2.90	5.23	0.0073
	Mo-Mo2	6	3.14	2.90		
Mo_2N	Mo-N	3.00	2.11	3.71	3.84	0.018
	Mo-Mo	4.04	2.84	3.98		

(Note: *for the EXAFS fitting in Table 2, S_0^2 is the amplitude reduction factor; CN is the coordination number; R is interatomic distance (the bond length between Mo central atoms and surrounding coordination atoms); σ^2 is Debye-Waller factor (a measure of thermal and static disorder in absorber-scatterer distances); ΔE_0 is edge-energy shift (the difference between the zero kinetic energy value of the sample and that of the theoretical model). R factor is used to value the goodness of the fitting. This value was fixed during EXAFS fitting, based on the known structure of Mo foil. Error bounds that characterize the structural parameters obtained by EXAFS spectroscopy were estimated as N ± 20%; R ± 1%; σ^2 ± 20%; ΔE_0 ± 20%*)

Supplementary Table 3. Summary of the atomic ratios of metal nitrides based on XPS results.

Sample	Element content (at.%)	
	Metal	Nitrogen
$ScN_{0.98}$	50.31	49.69
TiN	46.84	53.16
Ni_3N	75.87	24.13
YN	54.14	45.86
ZrN	53.26	46.74
Mo_2N	66.21	33.79
InN	50.56	49.44

Supplementary Table 4. The concentration of ions in natural seawater.

	No. 1 (g L^{-1})	No. 2 (g L^{-1})	No. 3 (g L^{-1})
K^+	0.4483	0.4635	0.4635
Na^+	10.3223	10.6761	10.3357
Mg^{2+}	1.1556	1.2226	1.2033
Ca^{2+}	0.3831	0.4106	0.3969
Cl^-	18.95	18.28	18.77
SO_4^{2-}	2.70	2.49	2.41

Supplementary Table 5. Comparison of electrochemical performance between Mo_2N and other HER electrocatalysts in natural seawater.

Catalyst	Loading (mg cm^{-2})	η (mV) at 10 mA cm^{-2}	Tafel slope (mV dec^{-1})	Stability	Ref.
P-$CoSe_2$	1.02	~360	N/A	N/A	*Nat. Commun.* 2018, 9:2533
Mo_5N_6	0.4	257	N/A	20 mA cm^{-2} @ 100 h	*ACS Nano* 2018, 12, 12761−12769
Cr_2O_3–CoO_x	2	~60	N/A	N/A	*Nat. Energy* 2023, 8, 264–272
CoSe	4.81	330	N/A	N/A	*Adv. Energy Mater.* 2018, 1801926
U–CNT–900	0.28	~680	~159	12 mA cm^{-2} @ 7 h	*Nanoscale* 2015, 7, 2306–2316
VS_2@V_2C	0.8	444	N/A	150 mA cm^{-2} @ 200 h	*Nanoscale*, 2020,12, 6176-6187
Ni-Mo-S/C	0.52	~460	N/A	N/A	*Sci. Adv.* 2015,1, e1500259
Fe-Co_2P	1	489	N/A	40 mA cm^{-2} @ 100 h	*J. Energy Chem.* 2021, 55, 92–101.
Mo_2C-MoP	1.71	346	173	13 mA cm^{-2} @ 16 h	*Electrochim. Acta* 2018, 281, 710–716
CoMoP@C	0.354	448	N/A	20 mA cm^{-2} @ 10 h	*Energy Environ. Sci.,* 2017, 10, 788–798
RuCo	N/A	387	107	150 mA cm^{-2} @ 12 h	*Electrochim. Acta* 2016, 208, 180–187
$PtNi_5$	0.255	380	119	10 mA cm^{-2} @ 12 h	*Appl. Surf. Sci.* 2017, 413, 360–365
Pt@mh-3D MXene	0.2	280	N/A	10 mA cm^{-2} @ 250 h	*Adv. Funct. Mater.*2020, 30, 1910028
$PtMo_{0.1}$	N/A	254.6	N/A	150 mA cm^{-2} @ 173 h	*RSC Adv.,* 2018, 8, 9423–9429
Pt-CoP	N/A	~300	N/A	25 mA cm^{-2} @ 24 h	*J. Mater. Chem. A,* 2020, 8, 11246–11254
Mo_2N	**1**	**311**	**107.46**	**10 mA cm^{-2} @ 1013 h**	***This work***

Supplementary Table 6. Summary of the amount of NH_4^+ generated with metal nitrides based on ^1H NMR spectra results.

Sample	Amount of NH_4^+ (nmol $mg_{catalyst}^{-1}$)
Mo_2N	69.70
Ni_3N	57.50
TiN	38.65
ZrN	23.60
$ScN_{0.98}$	9.51
InN	6.18
YN	2.38

Supplementary Table 7. Comparison of the performance of zero-gap membrane flow electrolysers with different non-noble metal cathodes.

Catalyst (cathode | anode)	Catalyst loading (cathode | anode, mg cm^{-2})	Membrane	Electrolyte	Cell temp (°C)	Performance	Stability	Energy Efficiency (@1A cm^{-2} %)	Ref.
MoS_2/CB | IrO_2	2.5 | 2.0	Nafion 117	Pure water	80	0.3 A cm^{-2} @1.9 V	0.35 A cm^{-2} @18 h	N/A	*Int. J. Hydrogen Energy* **2014**, 39, 20837-20843
FeMoS/C | Ir	4.0 | 2.0	Nafion 212	Pure water	80	1 A cm^{-2} @1.85 V	N/A	66.49	*ACS Catal.* **2020,** 10, 14336-14348
$Co_{59}Cu_{41}$ | IrO_2	N/A | 0.1	Nafion 212	Pure water	90	1 A cm^{-2} @1.97 V	1 A cm^{-2} @48 h	62.44	*Int. J. Energy Res.* **2020,** 44, 2833–2844
$Cu_{93.7}Mo_{6.3}$ | IrO_2	0.47 | 0.1	Nafion 212	Pure water	90	1 A cm^{-2} @2.0 V	N/A	61.50	Appl. Catal. B Environ. **2017,** 206, 608-616
$Cu_{44.4}Ni_{46}Mo_{9.6}$ | IrO_2	1.33 | 0.1	Nafion 212	Pure water	90	1 A cm^{-2} @1.8 V	1 A cm^{-2} @48 h	68.33	*J. Power Sources* **2021**, 506, 230200
$Ni_{78}P_{22}$ | IrO_2	N/A | 0.1	Nafion 212	Pure water	90	1 A cm^{-2} @1.96 V	N/A	62.76	*J. Alloys Compd.* **2021**, 506, 230200
Mo_3S_{13}/CB | Ir	3.0 | 2.0	Nafion 115	Pure water	80	1 A cm^{-2} @1.98 V	0.35 A cm^{-2} @24 h	62.12	*ChemSusChem* **2015,** 8, 3512-3519
MoS_2 | IrO_2	0.6 | 2.0	Nafion 117	Pure water	80	0.06 A cm^{-2} @2.0 V	0.67 A cm^{-2} @200 h	N/A	*Int. J. Hydrogen Energy* **2016**, 41, 13331-13340
MoSx/C | IrO_2	N/A | 0.1	Nafion 212	Pure water	90	0.37 A cm^{-2} @1.9 V	0.43 A cm^{-2} @4 h	N/A	*J. Power Sources* **2018**, 392, 69-78
FeS_2 | IrO_2	5.0 | 2.0	Nafion 115	Pure water	80	1 A cm^{-2} @2.10 V	N/A	58.57	*ACS Catal.* **2016**, 6, 2626-2631
MoS_2 | IrRuOx	0.14 | 3.0	Nafion 115	Pure water	90	1 A cm^{-2} @1.9 V	N/A	64.74	Appl. Catal. B Environ. **2022,** 313, 121458
Co_3O_4 | IrO_2	5.0 | 2.0	Nafion 117	Pure water	80	1 A cm^{-2} @2.4 V	1.5 A cm^{-2} @24 h	51.25	*Catal. Today* **2019,** 336, 161-168
Boron-Co | Ir	1.0 | 2.5	Nafion 117	Pure water	90	1 A cm^{-2} @2.1 V	N/A	58.57	*Int. J. Hydrogen Energy* **2010**, 35, 5043-5052
$Ni_{96}W_4$/Cu | IrO_2	N/A | 0.1	Nafion 212	Pure water	80	1 A cm^{-2} @1.88 V	N/A	65.43	*ACS Sustainable Chem. Eng.* **2019,** 7, 8265-8273
Mo_3S_{13}-NCNT | Ir	3.0 | 1.5	Nafion 212	Pure water	80	1 A cm^{-2} @1.92 V	1 A cm^{-2}@ 100 h	64.06	*Small* **2020**, 16, 2003161
CoP | IrO_2	1.0 | 2.5	Nafion 117	Pure water	50 °C 400 psi	1 A cm^{-2} @2.05 V	1.86 A cm^{-2} @1700 h	60.00	*Nat. Nanotechnol.* **2019,** 14, 1071-1074
M-$CoSe_{1.28}S_{0.72}$ | IrO_2	1.0 | 3.0	Nafion 115	Pure water	60	1 A cm^{-2} @1.79 V	1 A cm^{-2} @416 h	68.72	*Sci. Adv.* **2023,** 9, cadh2885
Cr_2O_3-CoO_x | Cr_2O_3-CoOx	4.0 | 4.0	Nafion 115	Seawater	60	1 A cm^{-2} @1.87 V	0.1 A cm^{-2} @100 h	65.77	*Nat. Energy* **2023,** 8, 264-272
Mo_2N | IrO_2	**1.0 | 1.0$_{Ir}$**	**Nafion 115**	**Simulated seawater**	**60**	**1 A cm^{-2} @1.867 V**	**1 A cm^{-2} @900 h**	**65.85**	***This work***

References

1. McKay, D., Hargreaves, J.S.J. & Howe, R.F. XPS evidence for molybdenum nitride formation in ZSM-5. *Catal. Lett.* **112**, 109-113 (2006).
2. Nyholm, R. & Martensson, N. Core level binding energies for the elements Zr-Te (Z=40-52). *J. Phys. C: Solid State Phys.* **13**, L279-L284 (1980).
3. Shebanova, O., Soignard, E. & McMillan, P.F. Compressibilities and phonon spectra of high-hardness transition metal-nitride materials. *High Press. Res.* **26**, 87-97 (2006).
4. Liu, H.-X. et al. Pt*n*–O*v* synergistic sites on MoO*x*/*γ*-Mo_2N heterostructure for low-temperature reverse water–gas shift reaction. *Nat. Commun.* **13** (2022).
5. Porte, L. Stoichiometric ScN and nitrogen deficient scandium nitride layers studied by photoelectron spectroscopy. *J. Phys. C: Solid State Phys.* **18**, 6701 (1985).
6. Milosev, I., Strehblow, H.H., Navinsek, B. & Metikos-Hukovic, M. Electrochemical and thermal oxidation of TiN coatings studied by XPS. *Surf. Interface Anal.* **23**, 529-539 (1995).
7. Wang, Y., Chen, L., Yu, X., Wang, Y. & Zheng, G. Superb Alkaline Hydrogen Evolution and Simultaneous Electricity Generation by Pt-Decorated Ni_3N Nanosheets. *Adv. Energy Mater.* **7**, 1601390 (2017).
8. De La Cruz, W., Díaz, J.A., Mancera, L., Takeuchi, N. & Soto, G. Yttrium nitride thin films grown by reactive laser ablation. *J. Phys. Chem. Solids* **64**, 2273-2279 (2003).
9. Milošev, I., Strehblow, H.-H., Gaberšček, M. & Navinšek, B. Electrochemical Oxidation of ZrN Hard (PVD) Coatings Studied by XPS. *Surf. Interface Anal.* **24**, 448-458 (1996).
10. Nagata, T., Koblmüller, G., Bierwagen, O., Gallinat, C.S. & Speck, J.S. Surface structure and chemical states of a-plane and c-plane InN films. *Appl. Phys. Lett.* **95**, 132104 (2009).
11. Muneshwar, T. & Cadien, K. Comparing XPS on bare and capped ZrN films grown by plasma enhanced ALD: Effect of ambient oxidation. *Appl. Surf. Sci.* **435**, 367-376 (2018).
12. Travaglini, G., Marabelli, F., Monnier, R., Kaldis, E. & Wachter, P. Electronic structure of ScN. *Phys. Rev. B* **34**, 3876-3882 (1986).
13. Stoehr, M., Shin, C.S., Petrov, I. & Greene, J.E. Raman scattering from TiNx($0.67 \leqslant x \leqslant 1.00$) single crystals grown on MgO(001). *J. Appl. Phys.* **110**, 083503 (2011).
14. Cheng, Y.H., Tay, B.K., Lau, S.P., Kupfer, H. & Richter, F. Substrate bias dependence of Raman spectra for TiN films deposited by filtered cathodic vacuum arc. *J. Appl. Phys.* **92**, 1845-1849 (2002).
15. Balogun, M.-S. et al. Three-dimensional nickel nitride (Ni_3N) nanosheets: free standing and flexible electrodes for lithium ion batteries and supercapacitors. *J. Mater. Chem. A* **4**, 9844-9849 (2016).
16. Zhang, N. et al. Electrochemical Oxidation of 5-Hydroxymethylfurfural on Nickel Nitride/Carbon Nanosheets: Reaction Pathway Determined by In Situ Sum Frequency Generation Vibrational Spectroscopy. *Angew. Chem. Int. Ed.* **58**, 15895-15903 (2019).
17. Du, L. et al. Sublimation crystal growth of yttrium nitride. *J. Cryst. Growth* **312**, 2896-2903 (2010).
18. Rizzo, A. et al. Reactive bipolar pulsed dual magnetron sputtering of ZrN films: The effect of duty cycle. *Appl. Surf. Sci.* **427**, 994-1002 (2018).
19. Yuan, Y. et al. Zirconium nitride catalysts surpass platinum for oxygen reduction. *Nat. Mater.* **19**, 282-286 (2020).
20. Madapu, K.K. & Dhara, S. Effect of strain relaxation and the Burstein–Moss energy shift on the optical properties of InN films grown in the self-seeded catalytic process. *CrystEngComm* **18**, 3114-3123 (2016).

21. Wang, J. et al. Synthesis and photoluminescence properties of europium doped Mg–Al layered double hydroxides intercalated with MoO_4^{2-} anions. *Solid State Sci.* **14**, 562-566 (2012).
22. Du, W., Shi, Y., Zhou, W., Yu, Y. & Zhang, B. Unveiling the In Situ Dissolution and Polymerization of Mo in Ni_4Mo Alloy for Promoting the Hydrogen Evolution Reaction. *Angew. Chem. Int. Ed.* **60**, 7051-7055 (2021).
23. Andersen, S.Z. et al. A rigorous electrochemical ammonia synthesis protocol with quantitative isotope measurements. *Nature* **570**, 504-508 (2019).
24. Li, J. et al. Ethylene-glycol ligand environment facilitates highly efficient hydrogen evolution of Pt/CoP through proton concentration and hydrogen spillover. *Energ Environ Sci* **12**, 2298-2304 (2019).
25. Li, J. et al. A fundamental viewpoint on the hydrogen spillover phenomenon of electrocatalytic hydrogen evolution. *Nat. Commun.* **12**, 3502 (2021).
26. Yang, B., Huang, T., Dou, Y. & Kong, W. Stoichiometry ratio-induced structural and electronic properties changes of TaN thin films prepared by reactive magnetron sputtering. *Mater. Sci. Semicond. Proc.* **170**, 107979 (2024).
27. Lv, C. et al. Defect Engineering Metal-Free Polymeric Carbon Nitride Electrocatalyst for Effective Nitrogen Fixation under Ambient Conditions. *Angew. Chem. Int. Ed.* **57**, 10246-10250 (2018).
28. Asanova, T.I. et al. A new approach towards the study of thermal decomposition and formation processes of nanoalloys: the double complex salt $[Pd(NH_3)_4][PtCl_6]$. *New J. Chem.* **42**, 5071-5082 (2018).
29. Beers, W.W. & McCarley, R.E. Synthesis, structure and reactivity of .beta.-molybdenum dichloride. *Inorg. Chem.* **24**, 472-475 (1985).
30. Hao, J.-H., Jiang, R., Yin, Y.-H., Wang, Y.-F. & Jin, Q.-H. Density functional theory study of chlorine adsorption on the Pt(111) surface. *Surf. Sci.* **617**, 233-236 (2013).